Clim Dyn (2012) 39:2307–2328
DOI 10.1007/s00382-011-1222-y

Recent summer precipitation trends in the Greater Horn of Africa and the emerging role of Indian Ocean sea surface temperature

A. Park Williams · Chris Funk · Joel Michaelsen · Sara A. Rauscher · Iain Robertson · Tommy H. G. Wils · Marcin Koprowski · Zewdu Eshetu · Neil J. Loader

Received: 5 August 2011 / Accepted: 10 October 2011 / Published online: 29 October 2011

Abstract We utilize a variety of climate datasets to examine impacts of two mechanisms on precipitation in the Greater Horn of Africa (GHA) during northern-hemisphere summer. First, surface-pressure gradients draw moist air toward the GHA from the tropical Atlantic Ocean and Congo Basin. Variability of the strength of these gradients strongly influences GHA precipitation totals and accounts for important phenomena such as the 1960s–1980s rainfall decline and devastating 1984 drought. Following the 1980s, precipitation variability became increasingly influenced by the southern tropical Indian Ocean (STIO) region. Within this region, increases in sea-surface temperature, evaporation, and precipitation are linked with increased exports of dry mid-tropospheric air from the STIO region toward the GHA. Convergence of dry air above the GHA reduces local convection and precipitation. It also produces a clockwise circulation response near the ground that reduces moisture transports from the Congo Basin. Because precipitation originating in the Congo Basin has a unique isotopic signature, records of moisture transports from the Congo Basin may be preserved in the isotopic composition of annual tree rings in the Ethiopian Highlands. A negative trend in tree-ring oxygen-18 during the past half century suggests a decline in the proportion of precipitation originating from the Congo Basin. This trend may not be part of a natural cycle that will soon rebound because climate models characterize Indian Ocean warming as a principal signature of greenhouse-gas induced climate change. We therefore expect surface warming in the STIO region to continue to negatively impact GHA precipitation during northern-hemisphere summer.

Keywords African monsoon · Indian Ocean warming · Drought · Moisture transports · Energy flux · Tree rings · Stable isotopes · Global warming · Food security

A. P. Williams (✉)
Earth and Environmental Sciences Division,
Los Alamos National Laboratory, Los Alamos, NM, USA
e-mail: parkwilliams@lanl.gov

A. P. Williams · C. Funk · J. Michaelsen
Geography Department, University of California,
Santa Barbara, CA, USA

C. Funk
Earth Resources Observation and Science (EROS),
U.S. Geological Survey, Sioux Falls, SD, USA

S. A. Rauscher
Theoretical Division,
Los Alamos National Laboratory, Los Alamos, NM, USA

I. Robertson · N. J. Loader
Department of Geography, College of Science,
Swansea University, Swansea, UK

T. H. G. Wils
Department of Geography, Rotterdam University,
Rotterdam, The Netherlands

M. Koprowski
Laboratory of Dendrochronology, Institute of Ecology
and Environment Protection, Nicolaus Copernicus University,
Toruń, Poland

Z. Eshetu
Forestry Research Centre, Ethiopian Institute of Agricultural
Research, Addis Ababa, Ethiopia

1 Introduction

At the eastern boundary of the Sahel lies the Greater Horn of Africa (GHA), a region of northeastern Africa with highly food-insecure countries that are particularly

vulnerable to interannual and decadal swings in precipitation totals (Funk et al. 2008; Funk and Brown 2009). Both the GHA and Sahel receive the bulk of their precipitation during the June–September (JJAS) boreal summer season. These regions experienced a significant decline in JJAS precipitation during the 1970s and 1980s due to anomalous warming of the South Atlantic and Indian Oceans (Folland et al. 1986; Hastenrath 1990; Giannini et al. 2003; Hoerling et al. 2006; Cook 2008) and subsequent shifts in moisture transports and upper-air flow (Nicholson 2000, 2009b; Nicholson and Grist 2003). Following the 1980s, warming in the North Atlantic appears to have caused a precipitation recovery throughout much of the Sahel (Giannini et al. 2008; Hagos and Cook 2008). In the GHA, however, the extent of post-drought recovery is unclear. Recent studies suggest drying over GHA may have continued into the 2000s (Seleshi and Zanke 2004; Funk et al. 2011b), but the cause of this potential drying and decoupling of precipitation trends in the GHA from those of the Sahel remains unexplored.

Previous studies have identified a variety of drivers of JJAS precipitation and drought in the GHA. While JJAS wind trajectories toward the GHA are quite variable from year to year, the rainforest region of the Congo Basin appears to be the main moisture source to Sudan and much of the Ethiopian Highlands, and the Indian Ocean is the main moisture source for eastern portions of Ethiopia and Kenya (Camberlin 1997; Gatebe et al. 1999; Riddle and Cook 2008; Levin et al. 2009). South of the center of the North African surface low, deep convection and enhanced moisture transport from the south and west fuel monsoonal precipitation during JJAS in the Sahel and GHA. Historically, for both the Sahel and GHA, the primary driver of interannual and longer-term variability of summer precipitation is the north-south displacement of jets, zone of maximum convection, and southern boundary of the thermal low over northern Africa (Nicholson 2009b), all of which appear to be influenced by tropical sea-surface temperature (SST) anomalies (Bhatt 1989; Whetton and Rutherfurd 1994; Camberlin 1995, 1997; Riddle and Cook 2008; Kucharski et al. 2009; Segele et al. 2009a). Some research also suggests that increased tropospheric aerosol concentration works to suppress the northward migration of the JJAS rainbelt into northern Africa, potentially reducing precipitation in the GHA (Rotstayn and Lohmann 2002). Further, relationships exist between the strength of the Indian monsoon and GHA precipitation (Camberlin 1997). Overall, drought in the GHA tends to occur when there is a reduction in the amount of moisture reaching the GHA from the tropical Atlantic Ocean and Congo Basin region.

Recently, a number of studies suggested that increased SSTs in the STIO may cause large-scale changes in atmospheric circulation and divert important moisture transports away from the GHA, altering previous relationships between regional circulation and precipitation (Verdin et al. 2005; Funk et al. 2008; Hagos and Cook 2008; Williams and Funk 2011). In an analysis of boreal spring (March–June, MAMJ), Williams and Funk (2011) found that higher SSTs in the STIO have driven large increases in convection and precipitation over the STIO. The resulting increase in the amount of diabatic energy released during precipitation has led to increased divergence of dry static energy (DSE) in the mid- and upper-troposphere. During MAMJ, this intensified outflow of mid- and upper-tropospheric DSE from the STIO has increased subsidence over northern Africa and decreased moisture transport into the GHA for at least the past 30 years. The decrease in the amount of moisture transported into the GHA region appears to have caused a reduction in what MAMJ precipitation totals would have otherwise been in the absence of increased SSTs in the STIO. Therefore, increased SSTs in the STIO and subsequent changes in moisture transports may signify a long-term alteration in how interannual variability in atmospheric circulation impacts interannual variability in precipitation totals throughout much of the GHA.

While no existing data sources detail the true sources of GHA precipitation, the composition of stable isotopes in Ethiopian rainwater suggests that most of the moisture is derived from the rainforests of the Congo Basin (Sonntag et al. 1979; Rozanski et al. 1996; Levin et al. 2009). Rainwater molecules in the Ethiopian Highlands and surrounding areas have exceptionally high levels of the heavy stable isotope of oxygen (^{18}O) (Dansgaard 1964; Levin et al. 2009). The high level of ^{18}O relative to ^{16}O (hereafter referred to using the standard $\delta^{18}O$ terminology) is evidence that the Congo Basin is a primary source of moisture to the GHA because moisture transpired by the wet forests of the Congo Basin does not undergo isotopic fractionation (Zimmermann et al. 1967; Salati et al. 1979; Gat and Matsui 1991). Unfortunately, isotopic records of precipitation throughout the GHA are inadequate to determine whether there is a trend in the proportion of precipitation coming from the humid continental interior. Conveniently, trees use rainwater to create cellulose during photosynthesis, and $\delta^{18}O$ in precipitation is partially conserved in cellulose (Yapp and Epstein 1982; Roden and Ehleringer 1999a; Roden et al. 2000; McCarroll and Loader 2004; Gessler et al. 2009). In trees that produce annual growth rings, the isotopic composition of cellulose in tree rings may reflect an annual record of $\delta^{18}O$ in precipitation (Roden and Ehleringer 1999a; Robertson et al. 2001; Anchukaitis and Evans 2010). We will investigate whether this is the case for trees in the Ethiopian Highlands.

In this study we use a unique network of over 1,200 publicly and privately available gauge records from

northern and eastern Africa to calculate a best-estimate record of JJAS precipitation for the GHA through 2009. Where sufficient precipitation data are available, we quantify the degree to which the GHA has recovered relative to the 1970–1989 mean. We then identify the atmospheric mechanisms that governed interannual variability in GHA precipitation during the period of 1948–1989 and determine whether the relationships between GHA precipitation and these mechanisms remained stable from 1990 to 2009. We utilize reanalysis climate data and a tree-ring isotope record from the Ethiopian Highlands to test the possibility that rapidly rising SSTs in the Indian Ocean have acted to suppress JJAS precipitation in the GHA following the peak of the Sahel drought in the 1980s.

2 Data and methods

2.1 Precipitation data

As the primary basis for evaluating precipitation trends throughout the Sahel and GHA, we use 0.25° spatial interpolation of a dense set of observational gauge precipitation records (Funk et al. 2003, 2007, 2011b; Funk and Michaelsen 2004; Funk and Verdin 2009). This dataset (CHG-CLIM) was developed by the Climate Hazards Group (CHG) at the University of California, Santa Barbara. The gridded product was constructed using quality-controlled rain-gauge data from 109 stations in Sudan, 210 stations in Ethiopia, 57 stations in Uganda, 144 stations in Kenya, and 817 stations throughout other Sahel and east African countries. Because the CHG is an active member of the Famine Early Warning Systems Network (FEWS NET) and routinely obtains and analyzes up-to-date meteorological records to support decision-making processes for food security, the CHG archive has substantially more recent observations than those found in standard global station archives. Figure 1 shows maps of mean gridded JJAS precipitation totals, gridded mean standard-error estimates, station locations, each station's percent of reported monthly JJAS data from 1948 to 2009, and a plot of the number of reporting stations in the Greater Horn region during each JJAS season. The CHG-CLIM dataset and underlying methodologies are described in detail in Funk et al. (2011b) and summarized in the "Appendix".

2.2 Seasonal precipitation record for the Greater Horn of Africa

We limit our region of focus to areas within Sudan, Ethiopia, Uganda, and Kenya (these countries are outlined in green in Fig. 1) where the following criteria are met: (1) mean JJAS precipitation during 1990–2009 is less than that of 1970–1989, (2) mean JJAS precipitation exceeds 75% of mean MAMJ precipitation, which is the dominant rainy season immediately south of our region of interest, and (3) mean JJAS precipitation exceeds 150 mm. The study area includes southern Sudan, western Ethiopia, northern Uganda, and parts of western Kenya. While the term "GHA" is generally used to refer to a quite larger region, we use the term to refer only to our study area defined here. Our GHA region is outlined in red in all map figures beginning with Fig. 2.

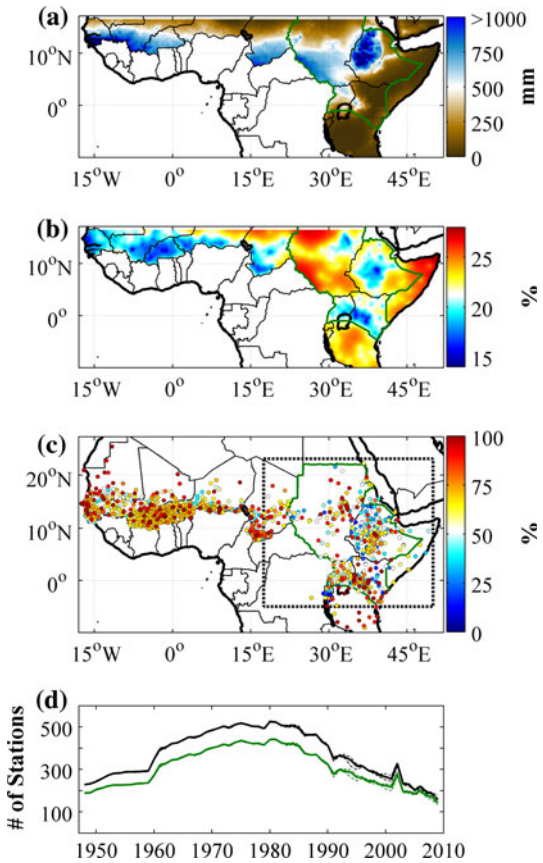

Fig. 1 CHG-CLIM precipitation during JJAS. **a** Mean total JJAS precipitation during 1948–2009. **b** Standard error reported as percent of mean. **c** Station locations and % of JJAS months from 1948 to 2009 with non-missing data. **d** Time series of the average number of stations reporting a monthly precipitation total for each of the JJAS months. *Dotted lines* bound the inner quartiles. The *black line* represents the number of stations within the *black box* in **c**. The *green line* represents the number of stations in the *green polygon* in **c**, which bounds Sudan, Ethiopia, Uganda, and Kenya

To calculate a time series of JJAS precipitation for the GHA, we first standardized (converted to z-scores) each grid cell's time series by subtracting its mean and dividing by its standard deviation. We then calculated the region's average standardized anomaly from each JJAS season during 1948–2009. The resulting time series of mean seasonal anomalies for the region accounts for 59% of the interseasonal variability throughout the region. This mean

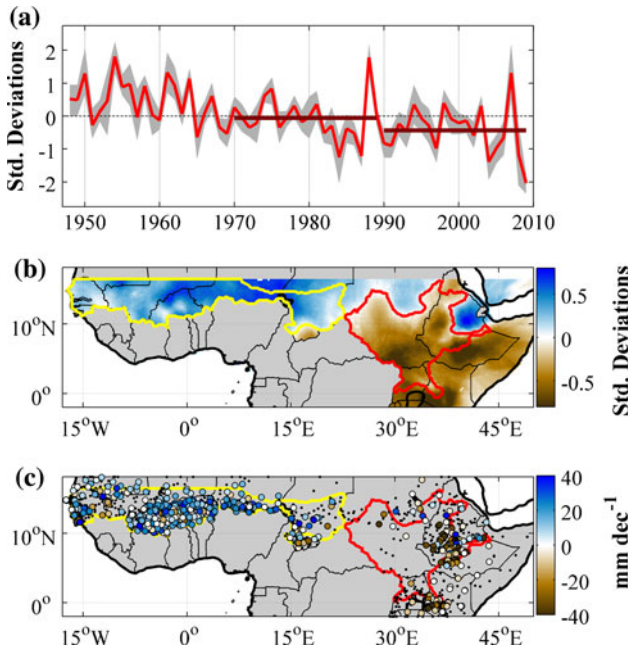

Fig. 2 **a** Time series of standardized (z-scores) seasonal JJAS precipitation totals within the GHA from 1948 to 2009. *Red line* is the mean regional record. *Grey area* bounds inner quartile values. *Heavy horizontal lines* represent means during 1970–1989 and 1990–2009. **b** Mean standardized JJAS precipitation during 1990–2009 minus mean standardized precipitation during 1970–1989. **c** Rate of precipitation change between 1970–1989 and 1990–2009 at all gauge locations with at least 10 reported JJAS precipitation totals during each period. *Black dots* represent gauge locations that do not meet this requirement. *Red polygons* in **b** and **c** bound the GHA region considered in this study. *Yellow polygons* in **b** and **c** bound the Sahel region considered in this study

precipitation time series is most representative of precipitation in the central portion of the GHA (r = 0.9) and less representative toward the boundaries (r = 0.6–0.7). Similar to what has already been established by several studies focusing on the Sahel (e.g., Nicholson 2009a), precipitation varies fairly ubiquitously across the GHA as a whole (i.e., wet seasons are wet everywhere and dry seasons are dry everywhere). Superimposed upon this regional mode of variability is a dipole-like pattern that causes the north and south to experience anomalies of opposite sign (hence the lower correlations near the boundaries). We explore sub-regional variability later in the drought-diagnostics portion of this paper.

It is crucial to this study that the CHG-CLIM data accurately reflect the direction of precipitation trends in the GHA following the Sahel precipitation decline that ended in the 1980s. Gaps in publicly available data and the cost of privately held data from eastern Africa, especially from Ethiopia, have caused previous studies to exclude parts of the GHA (e.g., Nicholson et al. 2003; Nicholson 2005). A recent study that employed data (137 gauge stations) purchased from the Ethiopian Meteorological Agency found good agreement with global gridded precipitation estimates for boreal summer months. The authors concluded that the purchased dataset is more accurate for Ethiopia than the global products, although they did not compare multi-decade trends among the various products (Dinku et al. 2008). The Ethiopian station data used in our study were also purchased from the Ethiopian Meteorological Agency, and are similar in quality and quantity to those examined by Dinku et al. (2008).

Given a shortage of literature on JJAS precipitation trends in the GHA following the Sahel drought, we compared our calculations of post-drought trends in the GHA to those of 10 alternate global precipitation products (Table 1). We used CHG-CLIM and each of the 10 alternate products to compare the direction and rate of change in JJAS precipitation in the GHA during the 1970–1989 period to that of the 1990–2009 period. For a wider regional perspective, we repeated this procedure for the Sahel region to the west (boundary outlined in yellow in Fig. 2b). We also evaluated precipitation trends in the GHA and Sahel from 1998 to 2009 using the satellite-derived Tropical Rainfall Measurement Mission (TRMM) 3B43 merged product (Kummerow et al. 2000). While TRMM 3B43 covers a shorter time period than the other data sets used here, it is useful for evaluating precipitation trends over the last decade because the amount of missing gauge data over the GHA increases during the same period (Nicholson 2005).

2.3 Precipitation and drought diagnostics

We used rotated principal components analysis (Richman 1986) to split the GHA into two (northern and southern) sub-regions. The sub-regional precipitation records accounted for 75% of variability in the north and 68% in the south.

In order to evaluate Indian Monsoon-GHA precipitation relationships (e.g., Camberlin 1997) we compared JJAS Bombay SLP to the north and south sub-regional CHG-CLIM precipitation time series using monthly station SLP data from the Global Historical Climate Network (GHCN, (ftp.ncdc.noaa.gov/pub/data/ghcn/v2/). If Bombay SLP did not adequately represent a regional precipitation record, we considered monthly SLP data from 1,107 alternate stations in Africa, southern Eurasia, and the Maritime Continent (see the "Appendix" for a description of SLP data processing). We calculated the correlation between precipitation and SLP at every pair of stations (including Bombay) from 1953 to 1988. We identified the pair of regions (clusters of stations) where SLP records could either be summed or subtracted to most accurately estimate JJAS precipitation.

We used three different reanalysis data sets to analyze how sub-regional precipitation variability is related to large-scale atmospheric circulation and vapor transports.

For the period 1948–1988 we used the NCEP/NCAR (Kalnay et al. 1996) and ECMWF ERA-40 (Uppala et al. 2005) reanalysis climate datasets. To test whether relationships established with SLP during 1948–1988 were stationary after the peak of the Sahel drought in 1988, we analyzed trends in both the original NCEP/NCAR reanalysis and NCEP-DOE Reanalysis 2 data (NCEP2, available for 1979–2009, Kanamitsu et al. 2002). NCEP2 uses an updated forecast model and data-assimilation system from the NCEP/NCAR reanalysis and it includes satellite data. We visualized trends in, and correlations with, wind-vector data using quiver-plot maps. In these maps, the *x*-axis of an arrow refers to the zonal (*u*) wind component and the *y*-axis refers to the meridional (*v*) wind component. In vertical profile maps depicting trends in, or correlations with, both horizontal and vertical wind velocity along a horizontal transect, the *x*-axis refers to the horizontal velocity component parallel to the transect and the *y*-axis refers to the vertical velocity component.

Informed by previous research (e.g., Gill 1980, 1982; Funk et al. 2008; Hagos and Cook 2008; Williams and Funk 2011), we investigated whether trends in Indian Ocean SSTs have impacted atmospheric circulation and moisture transports in ways that would influence GHA precipitation. We focused on the STIO region, defined here as 15°S–0°S, 55°E–90°E. We evaluated correlations between average JJAS SST in the STIO (NOAA extended SST reanalysis) and spatial fields of four variables: total cloud cover (NCEP2), net upward surface energy flux (NCEP2), dry static energy (DSE, NCEP2), and precipitation (GPCP v2.1). We calculated energy fluxes using definitions provided by Trenberth and Stepaniak (2003a). Net surface energy flux comprises the net upward radiation flux from the ocean's surface plus the upward fluxes of sensible and latent heat from the ocean's surface. DSE is the sum of the energy contained in the temperature and geopotential height of an air column.

We evaluated how higher SSTs in the STIO during recent decades have impacted interannual relationships between SLP and JJAS precipitation in the GHA. For each of the two GHA sub-regions, we classified JJAS seasons from 1948 to 2009 based upon whether SLP conditions were favorable for precipitation ("wet SLP" and "dry SLP"), and whether SSTs in the STIO were warm or cool. We designated all seasons with neutral SLP or SST conditions to a fifth "neutral" class. We evaluated mean JJAS precipitation (CHG-CLIM and Global Precipitation Climatology Centre (GPCC)) in the GHA during each of the five classes of seasons.

2.4 Moisture source information in tree-ring oxygen-18

At the compound of the Debrebirkan Selassie church in Gondar, Northwest Ethiopia (12°37′N, 37°29′E), 5 mm diameter cores were obtained from *Juniperus procera* trees in May 2007 as part of a larger sampling campaign (Wils et al. 2011). Successful cross-dating between 32 trees from five sites in the North Gondar zone was achieved by comparison of the wood anatomy directly on the surface of the samples and skeleton plotting (Stokes and Smiley 1968). Cross-dating was evaluated using the computer program COFECHA (Holmes 1983; Grissino-Mayer 2001) and the annual nature of the tree rings was confirmed by AMS radiocarbon dating (Wils et al. 2010, 2011).

Oxygen isotope ratios were measured on one tree core in a pilot study to obtain a preliminary insight into the potential environmental sensitivity of this isotopic variable in tree rings. Slivers were cut from absolutely dated annual growth rings representing years 1905–2003. Lignin was oxidized by the *in situ* generation of chlorine dioxide (ClO_2) and hemicelluloses were hydrolyzed from the resulting holocellulose to yield α-cellulose (Loader et al. 1997; Rinne et al. 2005). After sample homogenization, 0.30–0.35 mg of dry α-cellulose was weighted into silver vessels and pyrolysed over glassy carbon at 1,090°C. Oxygen isotope ratios were measured using a PDZ Europe 20-20 mass spectrometer interfaced to a Europa ANCA GSL elemental analyzer at Swansea University (Loader et al. 2008). Oxygen isotope ratios are expressed as per mille (‰) deviations relative to the VSMOW standard (Coplen 1995). Analytical precision was typically 0.3‰ as was illustrated by a repeat analysis of samples from 1910 (mean = 34.67‰, standard deviation = 0.3‰, n = 15).

Two influential variables on tree-ring $\delta^{18}O$ are the $\delta^{18}O$ of precipitation and the amount of isotopic enrichment of leaf water that occurs during transpiration (Roden and Ehleringer 1999a; Robertson et al. 2001; McCarroll and Loader 2004). Leaf-water enrichment is driven by the water vapor pressure deficit (VPD) of the atmosphere under a wide range of environmental conditions (Roden and Ehleringer 1999b). To test the impact of evaporative enrichment from leaves, we statistically regressed the tree-ring $\delta^{18}O$ record against monthly and multi-month VPD, as estimated by NCEP2 reanalysis. A positive relationship between tree-ring $\delta^{18}O$ and VPD would suggest evaporative enrichment is an important driver of interannual tree-ring $\delta^{18}O$ variability. A non-positive relationship would suggest tree-ring $\delta^{18}O$ variability is dominated by variations in $\delta^{18}O$ of precipitation.

We compared monthly NCEP2 reanalysis data to tree-ring $\delta^{18}O$ to test relationships between tree-ring $\delta^{18}O$ and variables suspected of influencing the source of precipitation in the GHA. Variables chosen were anti-cyclonic circulation of atmospheric moisture over the Gulf of Guinea and STIO. A good inverse proxy for anti-cyclonic moisture transports is cloud cover. For each month and range of months, we calculated the mean cloud frequency over the southern Gulf of

Table 1 Rate of precipitation change in the GHA and Sahel regions from the 1970–1989 period to the 1990–2009 period

Product name	Data years	Δ GHA precipitation (mm dec^{-1})	Δ Sahel precipitation (mm dec^{-1})	Reference
CHG-CLIM	1948–2009	−15.7	12.7	Funk et al. (2011b)
CMAP	1979–2009	−5.3	17.0	Xie and Arkin (1997)
CPC	1948–2009	−6.1	8.6	Chen et al. (2002)
CRU	1948–2009	1.9	21.3	Mitchell and Jones (2005)
ECMWF	1958–2001	−41.0*	−11.9*	Uppala et al. (2005)
GPCC	1948–2009	−4.1	9.4	Rudolf and Schneider (2005)
GPCP	1979–2009	4.5	41.7*	Adler et al. (2003)
MergPr	1948–2008	−1.9	−3	Smith et al. (2010)
NCEP/NCAR	1948–2009	−61.9*	−11.2	Kalnay et al. (1996)
NCEP2	1979–2009	−204.9*	1.3	Kanamitsu et al. (2002)
UDEL	1948–2008	−0.9	13.2	Willmott and Matsuura (1995)

* Significant ($P < 0.05$ from two-tailed t test) changes between time periods

Guinea (5°S–25°S, 15°W–20°E) and western STIO (2.5°S–10°S, 50°E–67.5°E). We then found the range of months when this cloud-cover correlated most strongly (and negatively) with tree-ring δ^{18}O. Exploratory analysis revealed that another good anti-cyclonic moisture transport index is the sum of meridional moisture transports over southern Africa to the east of the Gulf of Guinea (0°S–20°S, 15°E–30°E) and zonal moisture transports in the western STIO (2.5°S–10°S, 50°E–67.5°E). We repeated the analysis described above for this alternate index. For visualization of the more general circulation features associated with variability of tree-ring δ^{18}O, we also compared tree-ring δ^{18}O to the circulation fields evaluated throughout this study.

3 Results and discussion

3.1 JJAS precipitation during 1948–2009

JJAS precipitation declined substantially throughout much of the GHA during the 1948–2009 period. Figure 2a is a time series of standardized JJAS precipitation totals in the GHA region considered in this study, outlined in red in Fig. 2b, c. Declines during the 1960s–1980s occurred in concert with the well-known reductions throughout the Sahel (the Sahel region considered in this study is outlined in yellow in Fig. 2b, c). GHA precipitation decreased by approximately 1 standard deviation during the 1950–1989 period (Fig. 2a), corresponding to decreases of over 30 mm per decade throughout much of the Ethiopian Highlands, over 60 mm per decade in western Sudan, and little change in southern Sudan, northern Uganda, and western Kenya.

Following the 1980s, JJAS precipitation continued to decline in the GHA while there was no decline in precipitation throughout much of the Sahel region west of Sudan (Fig. 2). During 1990–2009, mean GHA precipitation was reduced by more than 0.5 standard deviation units compared to 1970–1989. Exceptions were observed in some areas in northeastern Ethiopia and northern Sudan, where post-1989 precipitation increased by over 0.5 standard deviation units. Notably, Fig. 14 in "Appendix" shows a similar spatial structure in recent precipitation trends for the MAMJ season. The similarity in spatial patterns of precipitation trends during JJAS and MAMJ suggests the same mechanism may be suppressing precipitation during both seasons despite the fact that the circulation patterns that *cause* precipitation during these two season are quite different.

Since station coverage has decreased over the past 20 years (Fig. 2c), we considered 10 alternate gridded estimates of JJAS precipitation in addition to our CHG-CLIM data. For the GHA and Sahel regions, Table 1 lists each additional dataset's rate of change in mean JJAS precipitation total comparing the 1970–1989 to the 1990–2009 period. Eight of the 10 alternate datasets agree with CHG-CLIM that JJAS precipitation did not increase in the GHA after the 1970–1989 period. For the Sahel region, 7 of 10 alternate datasets agree that 1990–2009 totals exceeded 1970–1989 totals. In addition, 9 out of 10 alternate datasets agree with CHG-CLIM that precipitation in the GHA either declined more or recovered less than in the Sahel. Notably, not all precipitation datasets cover the entire 1970–2009 period. If the negative post-1970 precipitation trend indicated by most datasets is real, datasets beginning in 1979 may indicate artificially low precipitation totals for 1970–1989 and datasets ending before 2009 may indicate artificially high totals for 1990–2009. Despite this bias, 5 of 6 datasets not covering the entire 1970–2009 still agree on reductions in GHA precipitation.

Finally, while the TRMM 3B43 data have limited temporal coverage compared to the other data sets, they indicate a substantial decline (~40%) in precipitation over the GHA and no change in the Sahel from 1998 to 2009 (Fig. 3). Although missing data surely hinder the accuracy

of interannual GHA precipitation estimates for all gauge-based datasets, particularly for the southern Sudan region (Fig. 2c), the broad consensus from the data considered here is that recovery from the drought in the 1970s and 1980s has been at least partially suppressed in the GHA relative to the Sahel.

3.2 Drivers of GHA precipitation and drought during 1948–1988

NCEP/NCAR and ECMWF reanalysis datasets suggest that JJAS vapor transports into the GHA primarily originate from the Atlantic Ocean (Fig. 4, see Fig. 15 in "Appendix" for the ECMWF figure). Transports into the GHA are almost entirely confined to the lower troposphere below 700 hPa and are likely recycled through the rainforests of the Congo Basin on their way from the Atlantic (Levin et al. 2009). Moisture in the Congo Basin appears to mainly originate from the Gulf of Guinea, driven by strong subtropical surface highs over the southern Atlantic and Indian Oceans and a strong low over northern Africa. Moisture is transported from the Congo Basin toward the GHA by low-level westerly and southwesterly winds, drawn into the region by thermally driven low surface pressures within the area of the Inter-Tropical Convergence Zone to the north and east into the GHA. There is substantial interannual variability in the amount of moisture entering the GHA via this pathway.

South of the center of the North African surface low, deep convection and enhanced moisture transports from the south and west drive monsoonal precipitation in the Sahel and GHA (Fig. 4c, d). For the Sahel, the primary driver of interannual and longer-term variability of JJAS precipitation is the north-south displacement of upper-level jet features, zone of maximum convection, and southern boundary of the thermal low over northern Africa (Nicholson 2009b). Wetter years occur when these features are displaced to the north. This rule was apparent in the northern GHA. From 1953 to 1988, northern GHA precipitation correlated very well ($r = 0.88$, $P < 0.0001$) with the SLP gradient between Sudan and the southeastern coast of the Mediterranean Sea (Fig. 5b). The rainiest seasons occurred when SLP was anomalously high in Sudan and anomalously low to the north in Egypt and surrounding countries (see Fig. 5a for SLP station locations and an outline of northern GHA). Variability in this SLP gradient explains interannual swings in JJAS precipitation as well as the Sahel-like decline in JJAS precipitation from the mid-1950s through mid-1980s over the GHA. For the southern GHA, JJAS precipitation correlated much more strongly with Bombay SLP ($r = -0.83$, $P < 0.0001$) during 1953–1988 (Fig. 5c). This corroborates the findings of Camberlin (1997), who, along with Hoskins and Rodwell (1995), hypothesized that diabatic heating associated with the Indian monsoon

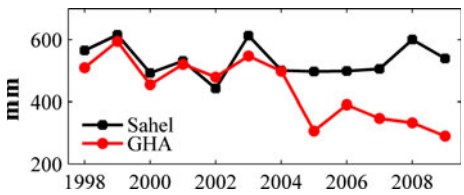

Fig. 3 Satellite-derived TRMM 3B43 mean regional JJAS precipitation totals within the GHA (*red*) and Sahel (*black*) from 1998 to 2009

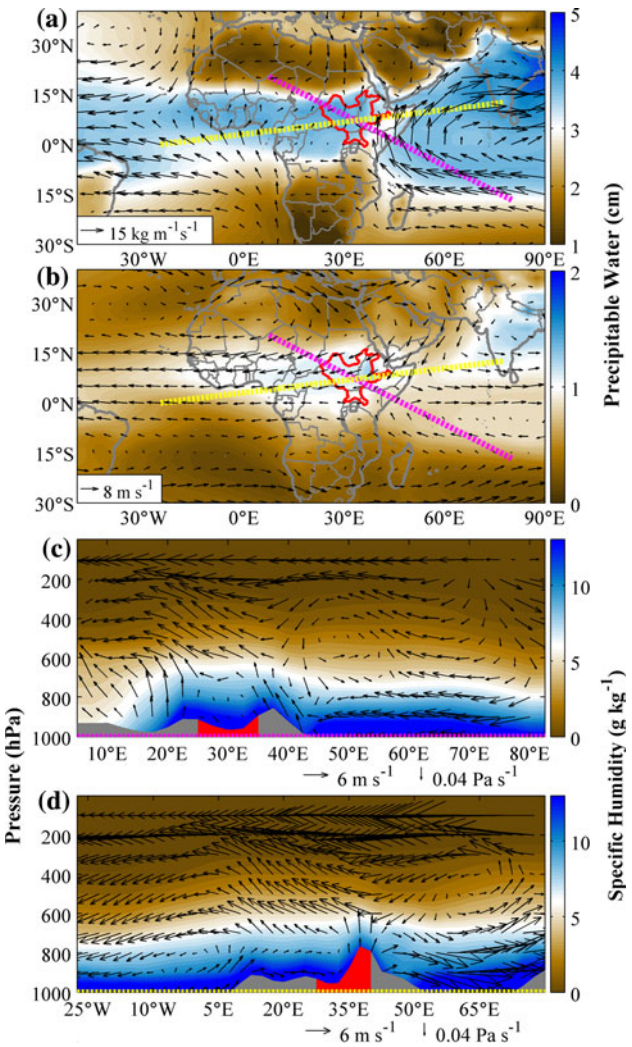

Fig. 4 Mean JJAS atmospheric circulation and moisture transports from 1958 to 2001 according to the NCEP/NCAR reanalysis. **a** Lower troposphere below 700 hPa: *arrows* indicate direction and velocity of moisture transports, background represents total precipitable water. **b** Mid-troposphere between 700 and 500 hPa: *arrows* indicate direction and velocity of wind, *background* represents total precipitable water. **c** and **d** Vertical profiles of horizontal and vertical wind velocity (*arrows*) and specific humidity (*background*) along the transects defined by the **c** *pink* and **d** *yellow dotted lines* in **a** and **b**. *Grey areas* at the bottom of (**c**) and (**d**) represent land. *Red outlines* in **a** and **b** and *red areas* in **c** and **d** represent the GHA

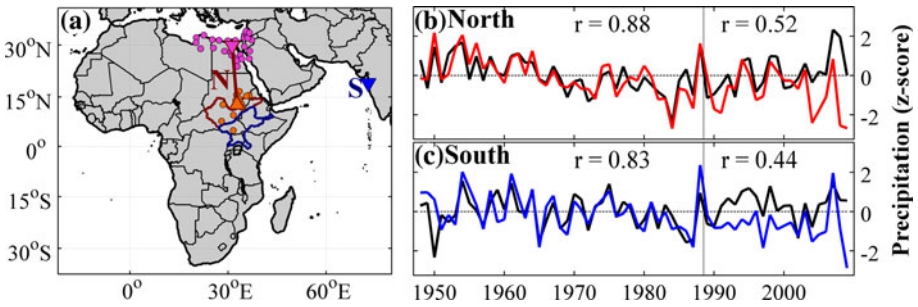

Fig. 5 **a** *Red* and *blue polygons* outline the northern and southern GHA sub-regions, respectively. Precipitation in the north was best described by the SLP gradient between high SLP at stations in Sudan (*orange dots*) and low SLP at stations in the southern Mediterranean area (*pink dots*). Precipitation in the southern region was best described by low SLP in Bombay (*blue triangle*). Up- and down-pointing triangles represent positive and negative relationships, respectively, between sub-regional precipitation and regional SLP. **b** Time series of standardized JJAS precipitation in the northern GHA (*red*) and estimated precipitation (*black*) using the linear relationship between the Sudan-to-Mediterranean SLP gradient and JJAS precipitation from 1948 to 1988. **c** Time series of standardized JJAS precipitation in the southern GHA (*blue*) and estimated precipitation (black) using the linear relationship between Bombay SLP and JJAS precipitation from 1948 to 1988. The *vertical grey lines* in **b** and **c** divide the pre-1988 and post-1988 portions of the time series

supported an intensified tropical easterly jet (TEJ) across Africa and a low-level response across Africa that involved ridging across the Sahara at ~25°N, surface lows around 12°N, and westerly wind toward the GHA.

NCEP/NCAR and ECMWF reanalyses support the idea that enhanced westerly transports across tropical Africa contribute to enhanced GHA precipitation (e.g., Camberlin 1997; Jury 2010). Figures 6 and 7 show correlation between various aspects of NCEP/NCAR atmospheric circulation (including moisture transports) and JJAS precipitation in the northern and southern GHA, respectively (see Figs. 15 and 16 in "Appendix" for duplications of these figures calculated with ECMWF). Northern GHA precipitation is correlated with a strong North African surface low and cyclonic southwesterly winds toward the GHA (Fig. 6a). Correlation with southwesterly wind velocity is not confined to the lower troposphere where the vast majority of water vapor is transported, but instead extends throughout all altitudes below the TEJ (Fig. 6b, d). Northern GHA precipitation is positively correlated with an enhanced TEJ (Fig. 6c, d). Both of these results are consistent with observations of a relatively weak African Easterly Jet and strong TEJ during wet monsoon seasons in the Sahel region (Kanamitsu and Krishnamurti 1978; Newell and Kidson 1984).

While correlations between reanalysis atmospheric circulation (including moisture transports) and JJAS precipitation in the southern GHA were weaker than for the northern GHA (Fig. 7), precipitation records for both regions correlate with moisture transport traveling from the Gulf of Guinea and across the Congo Basin (Fig. 7a, b, d). A main difference between drivers of north versus south GHA precipitation is that southwesterly cyclonic circulation is not necessary to deliver moist air to the southern GHA. Instead, southern GHA precipitation correlates with purely westerly flow across Africa between the surface and 500 hPa. This westerly flow is associated with enhanced surface low-pressure over western India and the western Indian Ocean north of Madagascar (Fig. 7a, b), consistent with the results of the SLP analysis. Southern GHA precipitation also correlated with ascending motion over western Africa and on the eastern boundary of the STIO (Fig. 7c, d). Correlations with ascending motion were particularly strong over the STIO and weaker over the GHA in the ECMWF analysis. In both reanalyses, correlation with ascending motion was generally confined to the mid- and upper-troposphere between 600 and 200 hPa. The correlation fields indicate that enhanced convection in rainy seasons corresponds with an enhanced TEJ, as was the case for northern GHA precipitation. Previous work has shown that an enhanced TEJ contributes to enhanced instability throughout the atmospheric column during the north African summer monsoon (Nicholson 2009b; Segele et al. 2009a, b).

3.3 Post-1988 climate trends and drought diagnostics

From 1989 to 2009, the SLP gradient between Sudan and the southern Mediterranean coast strengthened and Bombay SLP declined (Fig. 5b, c). According to the strong statistical relationships between SLP and GHA precipitation, these trends should be associated with increasing JJAS precipitation throughout the GHA region (north and south). The fact that GHA precipitation did not rebound following the 1980s suggests that a secondary factor worked to suppress it and alter the previously established relationships with SLP.

To diagnose these altered relationships, we evaluate trends in atmospheric circulation and moisture transports in recent decades. Figure 8 shows linear trends in atmospheric

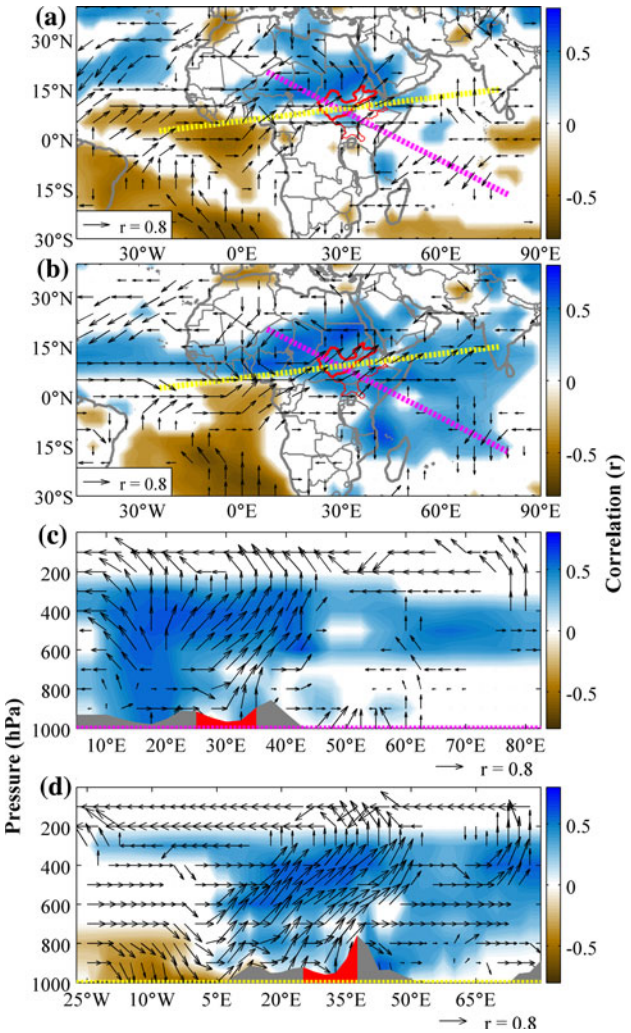

Fig. 6 Correlation between JJAS precipitation in the northern GHA and atmospheric circulation (including moisture transports) from 1948 to 1988 (NCEP/NCAR reanalysis). Only correlations exceeding the 90% significance level are shown. **a** Correlation with horizontal moisture transports (*arrows*) and specific humidity (*background*) within the lower troposphere below 700 hPa. **b** Correlation with horizontal wind velocity (*arrows*) and specific humidity (*background*) within the mid-troposphere between 700 and 500 hPa. **c** and **d** Vertical profiles of correlation with horizontal and vertical wind velocity (*arrows*) and specific humidity (*background*) along the transects defined by the *pink* (**c**) and *yellow* (**d**) *dotted lines* in **a** and **b**. *Arrows* in all plots represent correlation with velocity in zonal and meridional directions (**a** and **b**) or horizontal and vertical directions (**c** and **d**). Each *arrow* is the hypotenuse of an invisible triangle, of which the lengths of the *x*- and *y*-axes indicate the strength of correlation. *Grey areas* at the bottom of (**c**) and (**d**) represent land. *Bold red outlines* in **a** and **b** and *red areas* in **c** and **d** bound the northern GHA. *Thin red outlines* in **a** and **b** bound the rest of the GHA

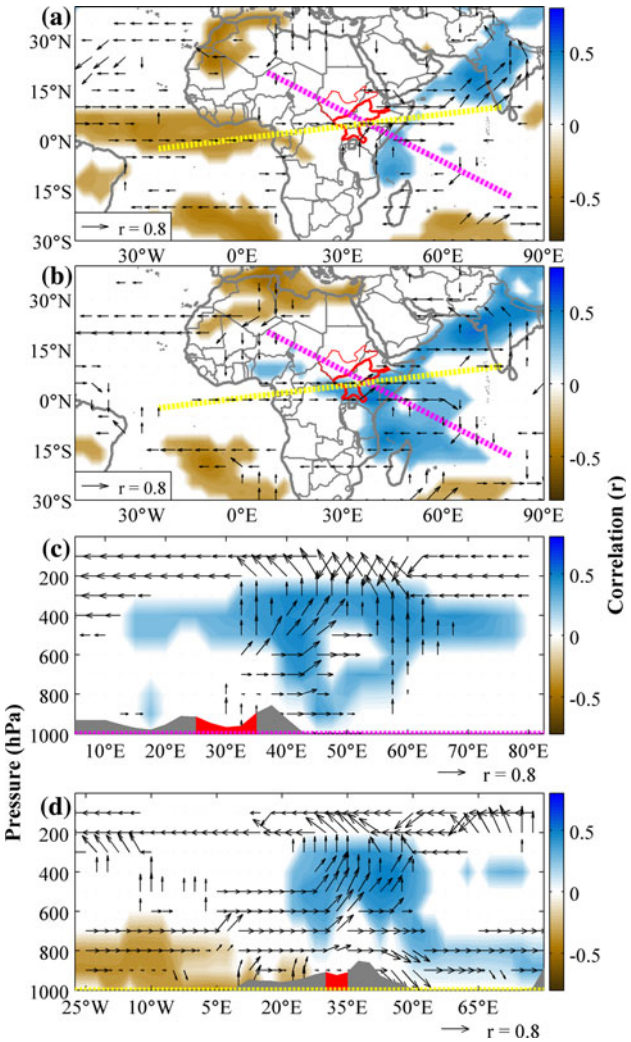

Fig. 7 Correlation between JJAS precipitation in the southern GHA and atmospheric circulation (including moisture transports) from 1948 to 1988 (NCEP/NCAR reanalysis). Only correlations exceeding the 90% significance level are shown. **a** Correlation with horizontal moisture transports (*arrows*) and specific humidity (*background*) within the lower troposphere below 700 hPa. **b** Correlation with horizontal wind velocity (*arrows*) and specific humidity (*background*) within the mid-troposphere between 700 and 500 hPa. **c** and **d** Vertical profiles of correlation with horizontal and vertical wind velocity (*arrows*) and specific humidity (*background*) along the transects defined by the *pink* (**c**) and *yellow* (**d**) *dotted lines* in **a** and **b**. *Arrows* in all plots represent correlation with velocity in zonal and meridional directions (**a** and **b**) or horizontal and vertical directions (**c** and **d**). Each *arrow* is the hypotenuse of an invisible triangle, of which the lengths of the *x*- and *y*-axes indicate the strength of correlation. *Grey areas* at the bottom of (**c**) and (**d**) represent land. *Bold red outlines* in **a** and **b** and *red areas* in **c** and **d** bound the southern GHA. *Thin red outlines* in **a** and **b** bound the rest of the GHA

circulation and moisture transports from 1979 to 2009, according to the NCEP2 reanalysis. Alternatively, see Fig. 18 in "Appendix" for differences between post- and pre-1988 periods rather than trends (calculated from the NCEP/NCAR reanalysis). Striking features in both figures are strong negative trend in convection and atmospheric water vapor content within and around the GHA. These negative trends appear to be linked to changes in SSTs and convection over the STIO (see Fig. 8c) that have been previously associated with negative precipitation trends

over the GHA during boreal spring (Funk et al. 2008; Williams and Funk 2011). In an analysis of the MAMJ season, Williams and Funk (2011) found that a westward extension of the Indian-Pacific tropical warm pool has led to a westward extension of the convective branch of the tropical Walker circulation over the STIO, and consequently, a westward migration of the western descending branch of the Walker system into northern Africa. Dynamically, increased SST in the STIO has driven large increases in convection and precipitation over the STIO, and the increase in the amount of diabatic energy released during precipitation has led to increased divergence of DSE in the overlying mid- and upper-troposphere. This intensified outflow of mid- and upper-tropospheric DSE from the STIO has caused increased subsidence over northern Africa and decreased moisture transports into the GHA for at least the past 30 years. Vertical velocity trends suggest similar mechanisms appear to be operating during the JJAS season (Fig. 8c, d).

The southeast-to-northwest overturning circulation trend displayed in Fig. 8c can be characterized as a single time series: the first principal component of all standardized time series of specific humidity, horizontal velocity, and vertical velocity represented in Fig. 8c in the geographic region between 30°E–80°E and the vertical region between the surface and 500 hPa. This principal component time series is plotted as the black line in Fig. 9a. In the same figure, the red line represents the seasonal JJAS time series of mean SST in the STIO region, calculated with the NOAA extended SST dataset. The overturning trend has been well correlated with STIO SST since at least 1979 ($r = 0.67$, $P < 0.0001$).

Also associated with the increase in SST over the STIO are increases in upward energy flux (Fig. 9b), cloud cover (Fig. 9c), and precipitation (Fig. 9d) within the STIO region. Since 1979, NCEP2 upward energy flux from the surface increased by approximately 43 W m^{-1} per °C in the STIO, NCEP2 cloud frequency increased by 5.9% per °C, and GPCP precipitation increased by 135 mm per °C. In the northwestern sub-section of the STIO (0°S–10°S, 55°E–75°E), GPCP precipitation increased by 295 mm per °C. Notably, there is considerable uncertainty in each of the calculations presented here because they pertain to derived, not measured, variables. There is, however, general corroboration from alternate datasets that the magnitudes of the above variables have all increased as STIO SSTs have increased (Table 2).

Increases in SST, upward energy flux, cloud cover, and precipitation over the STIO have been accompanied by diabatic heating in the mid-troposphere due to the conversion of latent energy into DSE during condensation (Trenberth and Stepaniak 2003b). Figure 9e shows that STIO surface warming corresponds with a significant

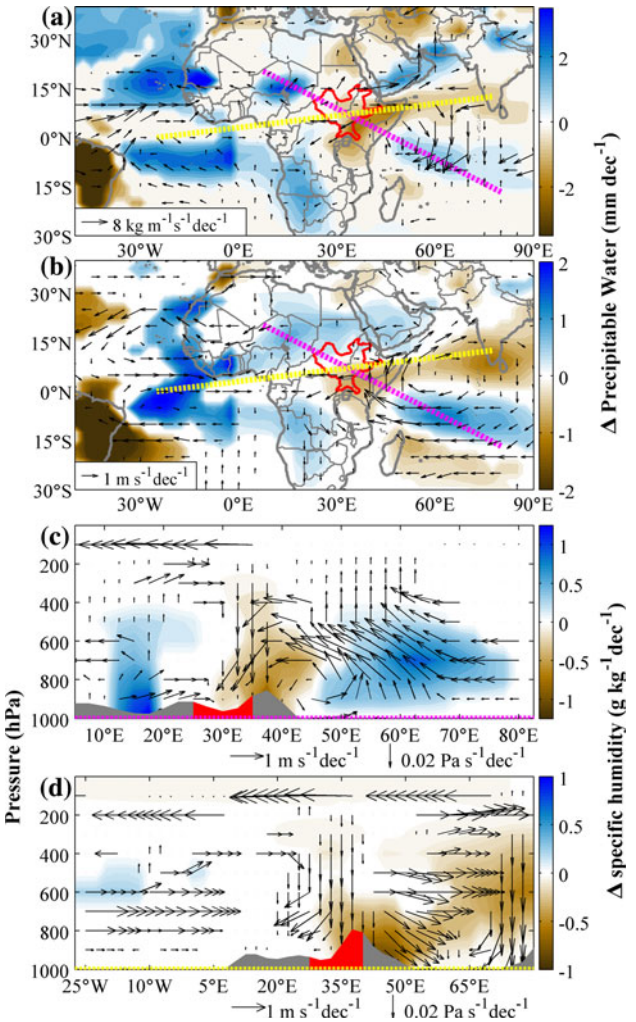

Fig. 8 Linear trends in JJAS atmospheric circulation and moisture transports from 1979 to 2009 (NCEP2 reanalysis). Only trends exceeding the 90% significance level are shown. **a** Trends in horizontal moisture transports (*arrows*) and specific humidity (*background*) within the lower troposphere below 700 hPa. **b** Trends in horizontal wind velocity (*arrows*) and specific humidity (*background*) within the mid-troposphere between 700 and 500 hPa. **c** and **d** Vertical profiles of trends in horizontal and vertical wind velocity (*arrows*) and specific humidity (*background*) along the transects defined by the *pink* (**c**) and *yellow* (**d**) *dotted lines* in **a** and **b**. *Grey areas* at the bottom of (**c**) and (**d**) represent land. *Bold red outlines* in **a** and **b** and *red areas* in **c** and **d** represent the GHA

increase in the amount of NCEP2 DSE exported from the region (56 Wm^{-2} per degree warming in the STIO). As was the case for GPCP precipitation, divergence of DSE increased most rapidly in the northwestern portion of the STIO. In this region, DSE correlated well ($r > 0.77$, $P < 0.0001$) with GPCP precipitation. Agreement between these two independently derived data sets, and their correlation with STIO SSTs, testifies to the strength of the inter-connection between STIO SSTs, precipitation in the STIO region, and the large-scale energetic response in the atmosphere.

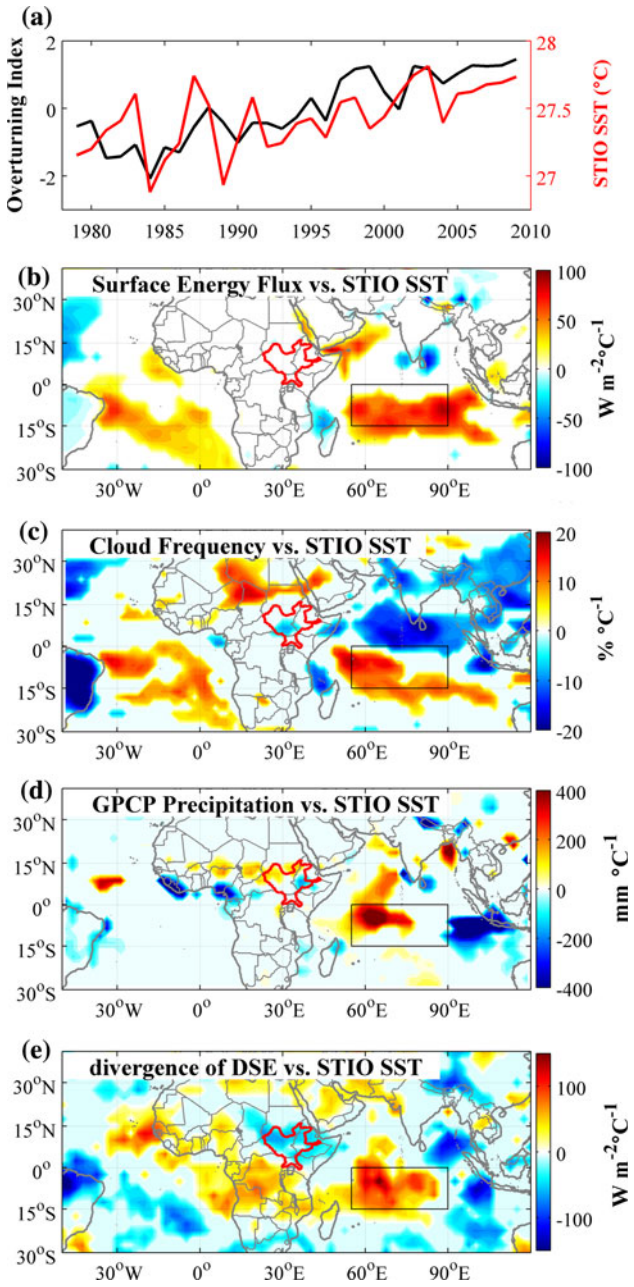

Fig. 9 **a** Standardized time series representing the overturning trend (*black*) shown in Fig. 8c east of 30°E and mean JJAS STIO SST (*red*). **b–d** Maps of linear relationships between JJAS STIO SST (*red line* in **a**) and **b** NCEP2 upward surface energy flux, **c** NCEP2 total cloud cover, **d** GPCP precipitation, and **e** NCEP2 divergence of DSE. *Black boxes* over the Indian Ocean bound the STIO region, *red outlines* bound the GHA

Increasing exports of DSE from the STIO region appear to be associated with increasing *imports* of DSE into the GHA (Fig. 9e). While Fig. 9e does not explicitly link divergence of DSE over the STIO to convergence of DSE over the GHA, the overturning trend shown in Fig. 8c does. This atmospheric response is in agreement with previous climate modeling work showing that an off-equatorial positive heating anomaly should lead to decreased convective activity over eastern Africa via a Gill-type response (e.g., Gill 1980, 1982; Funk et al. 2008). This is further supported by Fig. 8c, d, which shows that upward vertical velocities over the Ethiopian Highlands have slowed by as much as 0.06 Pa s^{-1} (a figure close to the climatological mean indicated in Fig. 4c, d). Finally, reduced convection over the GHA also reduces westerly moisture transport from the Congo Basin (Fig. 8b, d). This is particularly apparent in maps comparing mean states of atmospheric circulation during the 1948–1988 and 1989–2009 periods in Fig. 18b, d in "Appendix" .

Table 2 Regression of various calculations of JJAS energy flux, total cloud cover, and precipitation in the STIO (15°S–0°S, 55°E–90°E) versus NOAA JJAS SST in the STIO

Product name	Δ STIO energy flux (W m^{-2} °C^{-1})	Δ STIO cloud cover (% °C^{-1})	Δ STIO precipitation (mm °C^{-1})
CMAP	–	–	2
CPC	–	–	15
ECMWF	23	4.5	78*
GPCP	–	–	135*
MergPr	–	–	104*
NCEP/NCAR	32*	4.5*	219*
NCEP2	43*	5.9*	529*

* Significant ($P < 0.05$) relationships

3.4 Classification

To more carefully evaluate how STIO warming has influenced the spatial structure of JJAS precipitation in the GHA, we utilized the higher-resolution CHG-CLIM and GPCC interpolated precipitation products (Fig. 10 for north GHA, Fig. 11 for south GHA). In these figures, JJAS seasons from 1948 to 2009 are split into 5 unique classes based upon both the SLP record shown in Fig. 5 (Sudan-Mediterranean SLP gradient for north, Bombay SLP for south) and mean JJAS SST in the STIO. The 5 classes are (1) neutral, (2) wet SLP/cool STIO, (3) wet SLP/warm STIO (4) dry SLP/cool STIO, and (5) dry SLP/warm STIO. Neutral years were years when SLP and/or SST were within 1/8 of a standard deviation of the mean. Significantly more precipitation falls in "wet SLP" seasons than in "dry SLP" seasons in the north and south regions ($P < 0.0001$ and $P = 0.0012$, respectively). Among seasons classified as "wet SLP", the "warm STIO" seasons were significantly drier than the "cool STIO" seasons in the north and south ($P = 0.0478$ and 0.0094, respectively). Among seasons classified as "dry SLP", "warm STIO" seasons were marginally significantly drier than the "cool STIO" seasons in the north and south ($P = 0.0623$ and 0.0729, respectively).

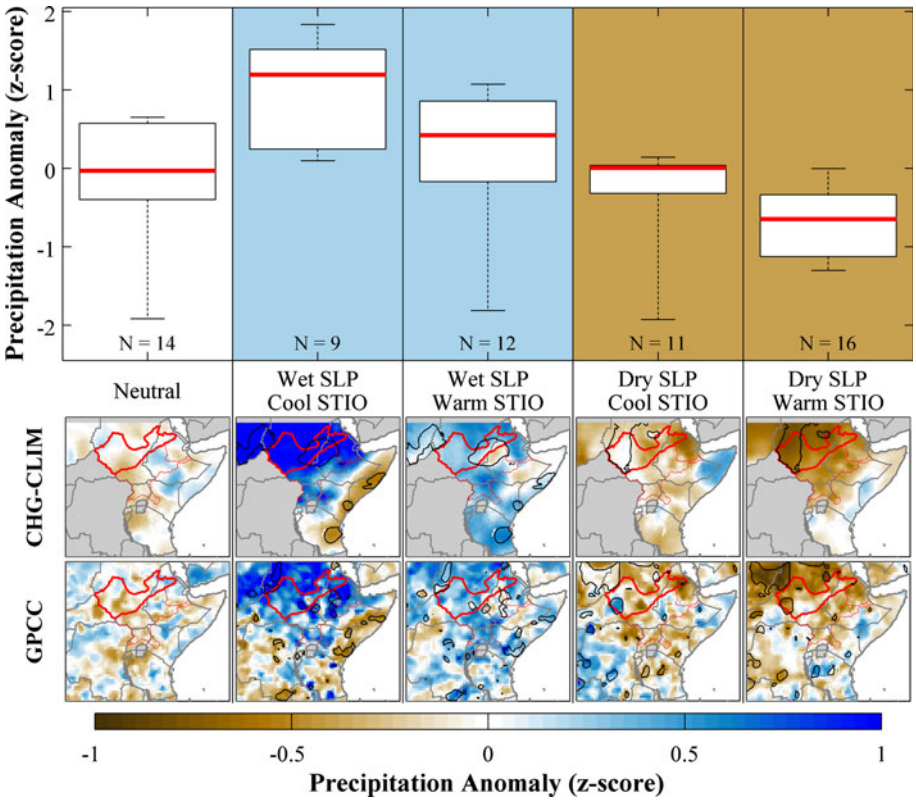

Fig. 10 (*Top*) Box plots of standardized JJAS precipitation totals in the northern GHA during five unique classes of seasons. Neutral seasons occurred when the Sudan-Mediterranean SLP gradient (Fig. 5b) and/or STIO SST (Fig. 9a) were within 1/8 standard deviations of the mean. Wet and dry SLP seasons occurred when the SLP gradient exceeded 1/8 standard deviations from the mean in the positive and negative direction, respectively. Warm and cool STIO seasons occurred when STIO SST exceeded 1/8 standard deviations from the mean in the positive and negative direction, respectively. Maps show mean precipitation calculated with CHG-CLIM (*top maps*) and GPCC (*bottom maps*) throughout northeastern Africa during each of the five classes of seasons. *Black contours* in maps bound areas where mean precipitation among wet or dry SLP seasons was significantly different (at >90% confidence level) between cool and warm STIO seasons

For each of the 5 classes, maps of mean CHG-CLIM (top) and GPCC (bottom) precipitation anomaly appear below the box plots in Figs. 10 and 11. It is clear from these maps that the regional tendencies described above generally hold throughout the GHA. The impact of increasing SSTs in the STIO appears to be particularly strong in the western Ethiopian Highlands, northern Uganda, and the Nairobi region of Kenya. In these regions, precipitation totals during "wet SLP/warm STIO" seasons are similar to, or even lower than, totals during "dry SLP/cool STIO" seasons (Fig. 11). This suggests that on a decadal scale, circulation dynamics associated with increasing SSTs in the STIO are becoming comparably important in dictating JJAS precipitation totals in the southern GHA as are the circulation dynamics associated with Bombay SLP variability. The relatively high gauge density throughout the Ethiopian Highlands, Uganda, and Nairobi regions (Fig. 1c) provides confidence that this finding is robust.

3.5 Tree-ring $\delta^{18}O$ and large-scale atmospheric circulation and moisture transports

The tree-ring $\delta^{18}O$ record is displayed in Fig. 12a (black line). Mean $\delta^{18}O$ from 1905 to 2003 was 32.8‰ with a standard deviation of 1.7‰. Values slowly declined by about 1‰ from 1905 to 1960 and then declined at a rate of 0.9‰ per decade from 1961 to 2003. Notably, this trend is not necessarily driven by climate change, as non-climate-driven age trends have been shown to occur naturally in tree-ring $\delta^{18}O$ records and can last for centuries (Esper et al. 2010). The negative $\delta^{18}O$ trend in our Ethiopian Highlands record, however, is an order of magnitude stronger than those observed by Esper et al. (2010). Further, recent work by Young et al. (2011) suggests that age trends in tree-ring $\delta^{18}O$ may not be significant in trees older than 50 years old. Nonetheless, more samples must be collected and measured to enhance the authority of interpretation of the strong negative $\delta^{18}O$ trend.

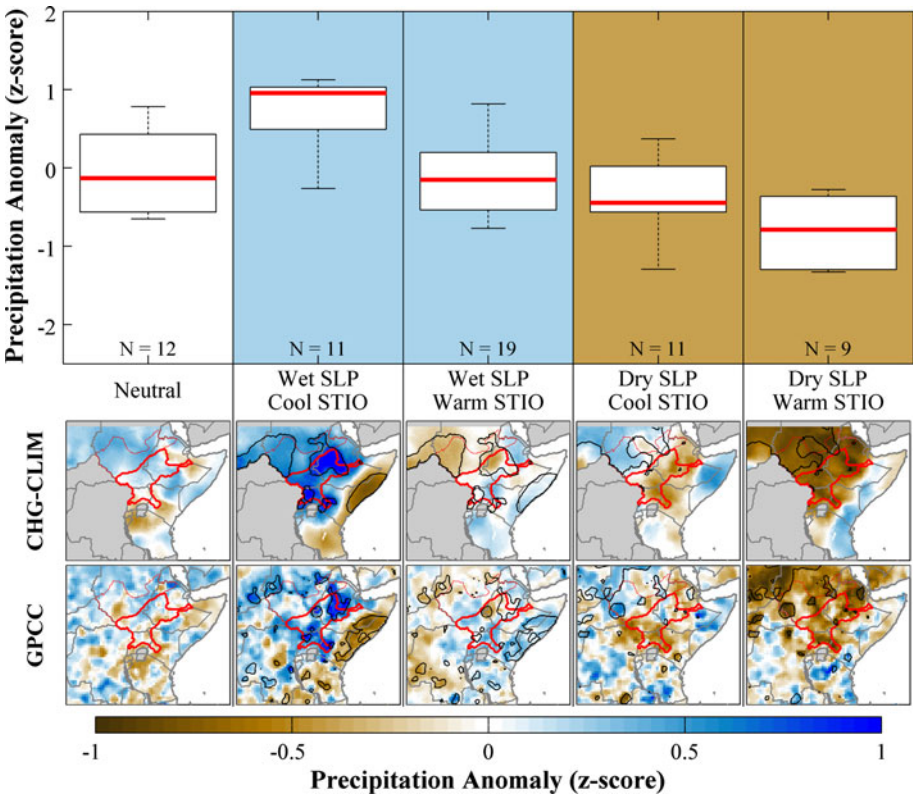

Fig. 11 (*Top*) Box plots of standardized JJAS precipitation totals in the southern GHA during five unique classes of seasons. Neutral seasons occurred when Bombay SLP (Fig. 5c) and/or STIO SST (Fig. 9a) were within 1/8 standard deviations of the mean. Wet and dry SLP seasons occurred when Bombay SLP exceeded 1/8 standard deviations from the mean in the negative and positive direction, respectively. Warm and cool STIO seasons occurred when STIO SST exceeded 1/8 standard deviations from the mean in the positive and negative direction, respectively. Maps show mean precipitation calculated with CHG-CLIM (*top maps*) and GPCC (*bottom maps*) throughout northeastern Africa during each of the five classes of seasons. *Black contours* in maps bound areas where mean precipitation among wet or dry SLP seasons was significantly different (at >90% confidence level) between cool and warm STIO seasons

Tree-ring $\delta^{18}O$ correlated positively but insignificantly with JJAS VPD during 1979–2003. Positive relationships were stronger when we considered VPD later in the growing season, but none were statistically significant. The weakness of the positive correlation is partly because VPD increased from 1979 to 2003 while $\delta^{18}O$ decreased. When linear trends are removed from $\delta^{18}O$ and VPD records, November-December VPD correlates with tree-ring $\delta^{18}O$ positively and significantly ($r = 0.51$, $P = 0.0099$). Maximum correlation with VPD probably occurs during November and December because this is when VPD finally grows large enough following the humid monsoon season to draw down soil moisture and cause evaporative fractionation within leaves as the tree increases its water-use efficiency.

The relatively weak relationships between $\delta^{18}O$ and VPD, and the opposing long-term trends, suggest tree-ring $\delta^{18}O$ may be influenced by a secondary climate factor in such a strong way as to offset the relationship between increasing VPD and evaporative enrichment. We hypothesized this secondary factor is the proportion of Highlands precipitation derived from the Congo Basin. This is an impossible variable to quantify, but an adequate proxy may be the sum of moisture transports entering the GHA from the Congo Basin area. Indeed, seasonal sums of vertically integrated zonal and meridional vapor transports (NCEP2) on the southwestern border of the GHA (2.5°N–5°N, 22.5°E–30°E) correlate positively and significantly with tree-ring $\delta^{18}O$ ($r = 0.48$, $P = 0.0144$). This relationship is no stronger than the relationship with VPD, however, because the moisture transport and $\delta^{18}O$ time series share a common trend.

The relatively weak relationship with southwesterly moisture transports may indeed indicate that the relationship is weak, or it may indicate that reanalysis moisture transport data insufficiently represent seasonal variability in the proportion of Highlands precipitation derived from the Congo Basin. Further correlation analyses supported the latter. Figure 13 shows correlations between tree-ring $\delta^{18}O$ and various components of large-scale atmospheric circulation during JJAS. In the STIO and southern Gulf of Guinea regions, anti-cyclonic circulation in the low- and

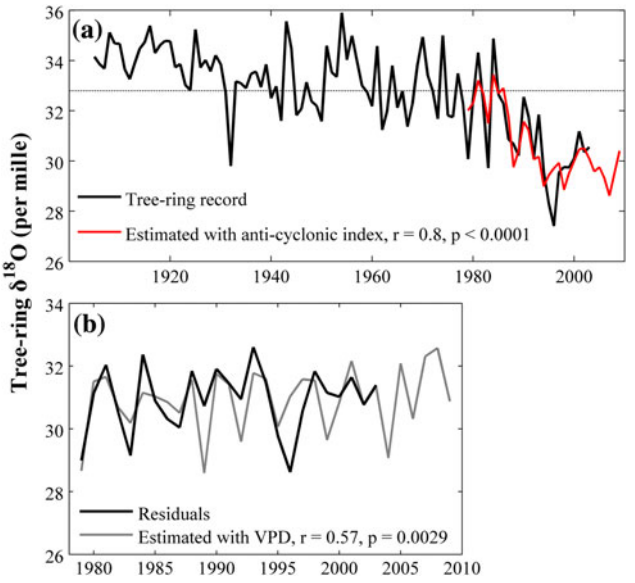

Fig. 12 **a** Tree-ring record of annual $\delta^{18}O$ (*black*) from Ethiopian Highlands and estimated $\delta^{18}O$ values (*red*) from the JJAS "anti-cyclonic index" for the STIO and southern Gulf of Guinea (NCEP2). The anti-cyclonic index is a standardized vapor-transport index minus a standardized cloud-cover index. The vapor-transport index is the sum of westerly vapor transports in the western STIO (2.5°S–10°S, 50°E–67.5°E) and southerly vapor transports east of the Gulf of Guinea (0°S–20°S, 15°E–30°E). The cloud-cover index is the sum of cloud frequency over the western STIO and southern Gulf of Guinea (5°S–25°S, 15°W–20°E). **b** Tree-ring $\delta^{18}O$ residual values (*black*) after the relationship with the anti-cyclonic index was removed. Estimated Residual values (*grey*) using reanalysis VPD data (NCEP2) at 12.5°N, 37.5°E, also adjusted to remove the relationship with the anti-cyclonic index

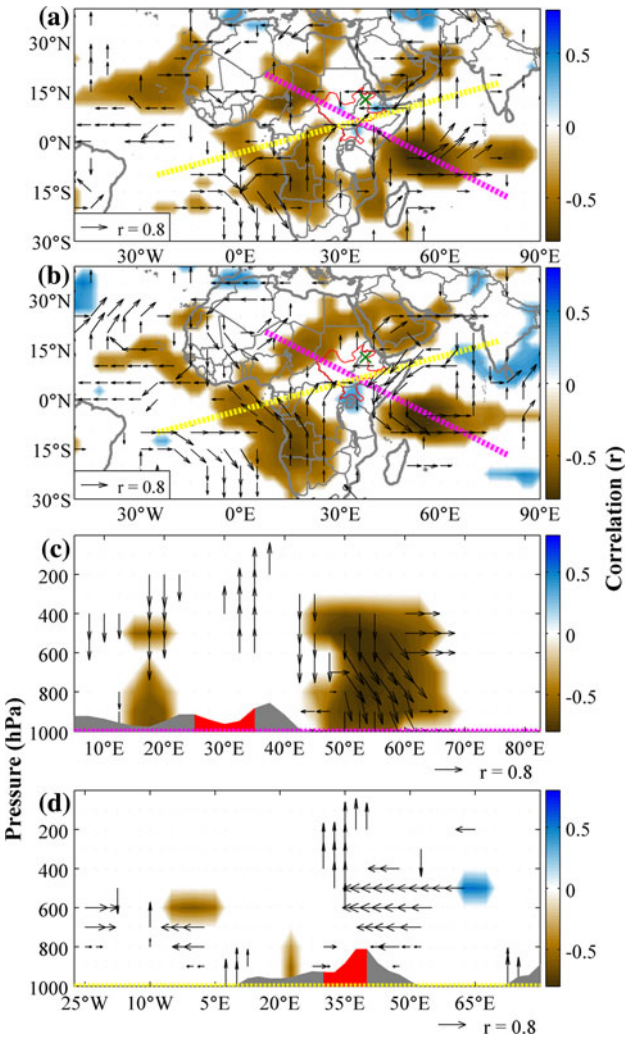

Fig. 13 Correlation between the tree-ring record of annual $\delta^{18}O$ and atmospheric circulation (including moisture transports) from 1979 to 2003 (NCEP2 reanalysis). Only correlations exceeding the 90% significance level are shown. **a** Correlation with horizontal moisture transports (*arrows*) and specific humidity (*background*) within the lower troposphere below 700 hPa. **b** Correlation with horizontal wind velocity (*arrows*) and specific humidity (*background*) within the mid-troposphere between 700 and 500 hPa. **c** and **d** Vertical profiles of correlation with horizontal and vertical wind velocity (*arrows*) and specific humidity (*background*) along the transects defined by the *pink* (**c**) and *yellow* (**d**) *dotted lines* in **a** and **b**. *Arrows* in all plots represent correlation with velocity in zonal and meridional directions (**a** and **b**) or horizontal and vertical directions (**c** and **d**). Each *arrow* is the hypotenuse of an invisible triangle, of which the lengths of the *x*- and *y*-axes indicate the strength of correlation. *Grey areas* at the bottom of (**c**) and (**d**) represent land. *Red lines* in **a** and **b** and *red areas* in **c** and **d** bound the GHA. The *green* "*x*" in Northwest Ethiopia (**a**) and (**b**) marks the location where the tree-ring $\delta^{18}O$ record was collected

mid-troposphere, descending motion, and low specific humidity all correlate significantly with tree-ring $\delta^{18}O$. The correlation pattern over the STIO is consistent with our hypothesis that increased convergence and convection in this region ultimately lead to decreased moisture transports from the Congo Basin into the GHA. The correlation pattern over the southern Gulf of Guinea supports previous research indicating that intensification of the surface high in this region drives intensified southwesterly moisture transports toward the GHA (Segele et al. 2009a).

An all-encompassing representation of anti-cyclonic anomalies in these regions is total cloud cover, which is derived from satellite data in the NCEP2 reanalysis. The sum of JJAS cloud frequency within the southern Gulf of Guinea (5°S–25°S, 15°W–20°E) and western STIO (2.5°S–10°S, 50°E–67.5°E) regions correlated negatively and significantly with tree-ring $\delta^{18}O$ ($r = -0.71$, $P < 0.0001$) during 1979–2003. JJAS was also the range of months when this cloud-cover index correlated most strongly with $\delta^{18}O$. Importantly, the strength of this negative relationship is not solely due to contrasting long-term trends. When linear trends were removed from both time series, correlation was still negative and significant ($r = -0.60$, $P = 0.0017$).

Further, the amount of anomalous vapor flow away from these regions represents how the anti-cyclonic anomalies relate to moisture transports from the Congo Basin toward

the GHA. The maps in Fig. 13a, b indicate that $\delta^{18}O$ is positively correlated with westerly vapor transports away from the STIO as well as southerly anomalies immediately to the east of the Gulf of Guinea, which at the equator turn into southwesterly anomalies toward the GHA. When vertically integrated JJAS zonal vapor transports over the western STIO (2.5°S–10°S, 50°E–67.5°E) are added to vertically integrated JJAS meridional vapor transports to the east of the Gulf of Guinea (0°S–20°S, 15°E–30°E), this vapor transport index correlates positively and significantly with tree-ring $\delta^{18}O$ ($r = 0.72$, $P < 0.0001$). The correlation strengthened when only the July–September period was considered ($r = 0.76$, $P < 0.0001$). Detrended, these time series still correlate positively and significantly (for JJAS, $r = 0.66$, $P = 0.0003$).

Because the indices of cloud cover and vapor transports for the STIO and southern Gulf of Guinea correlated far more strongly with tree-ring $\delta^{18}O$ than did VPD, we treated a combination of these two time series as the primary predictor of $\delta^{18}O$ (red line in Fig. 12a). This time series of the standardized vapor-transport record minus the standardized cloud-cover record, termed the "anti-cyclonic index," correlates better with $\delta^{18}O$ than does either record independently ($r = 0.80$, $P < 0.0001$). After correlation with the anti-cyclonic index was accounted for, the residual $\delta^{18}O$ record correlated positively and significantly with November-December VPD ($r = 0.57$, $P = 0.0029$, Fig. 12b).

This analysis is suggestive of a powerful link between increasing temperatures, evaporation, convection, precipitation, and divergence of DSE in the STIO and declining moisture transports from the Congo Basin toward the GHA. This serves as a call to action for the collection and measurement of additional tree-ring $\delta^{18}O$ records from the Ethiopian Highlands, as tree-ring $\delta^{18}O$ may hold valuable clues about historical variability in the source of moisture and how that variability has related to large-scale climate forcing.

4 Conclusions

As pressure on earth's resources increases, identifying and understanding decadal climate variations will become increasingly important. While work with global climate models will certainly continue to be very important, "forensic climatology" that analyzes the cause of observed droughts is another critical mode of inquiry. We show the GHA is a prime target for such inquiry because this region has experienced a declining trend in summertime monsoonal precipitation for approximately the past 60 years (Figs. 2 and 5). JJAS precipitation was particularly low in 2008 and 2009, causing the US government to spend over $2.3 billion on food aid in Sudan, Ethiopia, Kenya, and Uganda.[1] At present, parts of the GHA are in the midst of their lowest annual rainfall year in at least the past 60 years,[2] contributing to steep increases in food prices and child malnutrition.[3] On a longer time scale, lake-bed pollen records link precipitation variability in tropical eastern Africa with several major fluctuations in the amount of forest cover since the last glacial maximum (Bonnefille and Chalié 2000). It is therefore clear that GHA precipitation totals are capable of undergoing extreme low-frequency swings, likely in response to alterations in large-scale ocean and atmospheric circulations.

To gain insight into whether ongoing precipitation declines in the GHA can be expected to continue or rebound in coming decades, we compared records of GHA precipitation from 1948 to 2009 to records of large-scale atmospheric circulation. During the classic Sahel precipitation decline that ended in the late 1980s, precipitation in the northern GHA correlated very strongly with the sea-level pressure (SLP) gradient between Sudan and the southern coast of the Mediterranean Sea ($r = 0.86$, 1948–1988). Variability in this SLP gradient during 1948–1988 corresponds with the multi-decade decline in precipitation across the Sahel and GHA, and also corresponds with interannual variations specific to the northern GHA. In particular, the devastating drought year of 1984, which led to the deaths of at least several hundreds of thousands of Ethiopians and Sudanese (De Waal 1989; Kidane 1989), is clearly indicated by a weak Sudan-Mediterranean SLP gradient (Fig. 5b). For the southern GHA, 1948–1988 precipitation correlated negatively ($r = -0.83$) with average SLP in Bombay (Fig. 5c). These results indicate that prior to and during the Sahel drought, the strength of the summer monsoon in much of the GHA was strongly associated with the same large-scale climate processes that governed the strength of the monsoon throughout much of the Sahel to the west.

Notably, relationships between regional precipitation and these SLP indices have weakened in recent years. During 1990–2009, mean JJAS rainfall totals in the north and south GHA continued to decline even though the SLP indices discussed above trended in directions associated with more favorable precipitation conditions (Fig. 5). Evaluations of recent trends in atmospheric circulation and moisture transports (Fig. 8) suggest that warming in the STIO accounts for a substantial portion of these recent rainfall declines. Given strong and consistent surface winds in the

[1] http://www.usaid.gov/our_work/humanitarian_assistance/ffp/wherewework.html. Estimates based upon data available in May 2011.

[2] http://www.fews.net/docs/Publications/FEWS%20NET%20EA_Historical%20drought%20context_061411.pdf.

[3] http://www.fews.net/docs/Publications/Horn_of_Africa_Drought_2011_06.pdf.

STIO, and the already warm SSTs in this region, surface warming in the STIO during the past half century has led to large increases in STIO evaporation. Increased evaporation has dramatically increased the vertical flux of energy into the STIO atmosphere. This change has been accompanied by increases in STIO precipitation and the export of dry static energy (DSE) toward eastern Africa (Fig. 9). These DSE exports have had two negative impacts on GHA rainfall. First, they have increased DSE convergence over the GHA, increasing atmospheric stability and subsidence. Increased convergence of DSE over the GHA has had a secondary (but not necessarily less important) impact on westerly moisture transports from the Congo Basin. As DSE divergence has increased over the STIO and convergence of DSE increased over the GHA (Fig. 9e), ridging over the GHA has reduced moisture transport toward the GHA from the Congo Basin (Fig. 8, Fig. 18 in "Appendix").

Unfortunately, long observational records do not exist to tell us whether moisture transports from the moist Congo Basin have truly been redirected away from the GHA. Our analysis suggests, however, that clues may exist in the stable isotopic composition of annual growth rings in trees from the Ethiopian Highlands. While tree-ring $\delta^{18}O$ is often positively influenced by warm, dry conditions due to evaporative enrichment of leaf water, our analysis indicates that these conditions have only a secondary impact on tree-ring $\delta^{18}O$. We found that large-scale circulation features that affect transport of isotopically enriched atmospheric moisture from the Congo Basin toward the GHA are the primary influences on tree-ring $\delta^{18}O$ (Figs. 12 and 13). While this finding comes from only one tree and replication from additional samples will be crucial, this tree-ring analysis corroborates our other findings and may serve as a novel approach toward providing an answer to the difficult and complicated question of how large-scale climate variability impacts moisture transports into the GHA.

According to the latest report by the Intergovernmental Panel on Climate Change, observations of decreased JJAS precipitation in the GHA are in contrast to model projections of unchanged summer precipitation (Christiansen et al. 2007). Importantly, there is high uncertainty in model projections of precipitation and high variability among models regarding projections of precipitation in the GHA (Christiansen et al. 2007). While these models do not converge upon a connection between JJAS precipitation in the GHA and greenhouse-gas induced global climate change, data presented here suggest recent (post-1980s) drying trends can be largely attributed to a cascade of climate changes linked to warming trends in the STIO. Climate modeling studies implicate greenhouse gas and aerosol emissions as the primary causes of recent STIO surface warming (Pierce et al. 2006; Alory et al. 2007). Although warming-induced increases in evaporation and cloud cover work to dampen surface warming (Du and Xie 2008), climate models predict tropical Indian Ocean SSTs will continue increasing (Meehl et al. 2007). Resulting increases in evaporation, rainfall, and divergence of DSE in the STIO region (Fig. 9) are linked to diminished rainfall in the GHA following the classic Sahel drought of the 1970s and 1980s (Fig. 2). Unfortunately, these declines have occurred in extremely fragile and water-insecure regions where they have likely exacerbated social conflict (Funk et al. 2011a) and drought-induced forest mortality (Allen et al. 2010). The fact that swings in precipitation appear to have significantly impacted forest cover in the past (Bonnefille and Chalié 2000) suggests that GHA forest cover is at risk of decline due to declining JJAS precipitation. Beyond the direct influence that water shortage has on humans in the GHA, drought-driven forest mortality in the Ethiopian Highlands and Ugandan rainforest would likely have indirect effects on humans by influencing regional climate, the global carbon balance, and human access to important natural resources.

Acknowledgments This research was supported by the U.S. Agency for International Development Famine Early Warning System Network under U.S. Geological Survey Cooperative Agreement #G09AC00001 and the National Aeronautics and Space Administration under Precipitation Science Grant #NNX07AG266. Park Williams and Sara Rauscher gratefully acknowledge support from the U.S. Department of Energy through the LANL/LDRD Program. Iain Robertson is supported by the Climate Change Consortium of Wales. Marcin Koprowski was supported by an International Incoming Short Visit from the Royal Society (UK). Ethiopian precipitation data were provided by the Ethiopian Meteorological Agency. Thanks to Tufa Dinku for assisting the authors in obtaining this data purchase, providing the best possible foundation for an analysis of trends in Ethiopia. Thanks to Greg Husak for his invaluable part in obtaining CHG funding. Comments by Amy McNally, Brian Osborn, Charles Jones, Ellen Mosley-Thompson, Harikishan Jayanthi, Kevin Anchukaitis, Kyle Cavanaugh, Leila Carvalho, Lonnie Thompson, Naomi Levin, Tom Adamson, and two anonymous reviewers greatly improved the quality of the manuscript. NCEP/NCAR data were accessed online through the NOAA Earth System Research Laboratory (ESRL) Physical Sciences Division (PSD, http://www.esrl.noaa.gov/psd). ECMWF data were produced by the European Centre for Medium-Range Weather Forecasts ERA-40 project (http://www.data.ecmwf.int/data/). GHCN data were accessed from the National Climate Data Center (ftp://ncdc.noaa.gov/pub/data/ghcn/v2/).

Appendix

CHG-CLIM precipitation dataset

CHG-CLIM is produced in two steps: first monthly long-term mean fields are created, representing the *spatial*

variation of the data; then seasonal station anomalies are interpolated representing the *temporal* variations. JJAS rainfall climatologies are produced using moving window regressions, long-term (1960–1989) mean in situ observations, and background images of predictors (Funk et al. 2011b). The main predictors used are long-term averages of satellite rainfall estimates and land surface temperature retrievals. Because these fields directly relate to hydrologic processes in the semi-tropics, they provide a great deal of information about long-term mean rainfall. Latitude, longitude, and elevation are used as physiographic predictors. The at-station differences between the moving window regressions and average gauge observations are then interpolated using kriging (a geostatistical interpolation approach in which optimal interpolation weights are determined by the spatial covariance structure of the observed data), producing the final rainfall climatology along with the associated kriging standard errors.

Seasonal (JJAS) at-station percent anomalies were then interpolated using kriging (Journel and Huijbregts 1978). Using anomalies helps mitigate the impacts of changes in the reporting network. Square roots of rainfall percents are used to minimize the effects of skewness. Interpolation is carried out based on the spatial semivariogram, which depicts the relationship between inter-station distances and the inter-station covariances. This semivariogram is estimated based on the average of the 30 1960–1989 variograms. Interpolation via kriging produces 0.25° estimates of percent rainfall, and the associated kriging standard errors, in units of percent rainfall. The average 1948–2009 kriging standard errors are less than 25% for regions evaluated here. These percentage anomalies and standard errors were multiplied by the rainfall climatology to produce rainfall and standard error estimates in mm per season. While the year-to-year variability in the region is substantial, the coherent spatial covariance and reasonably dense gauge density combine to produce reasonably accurate depictions of rainfall. The CHG-CLIM dataset is discussed in greater detail in Funk et al. (2011b).

GHCN SLP records

There are many data gaps in the monthly GHCN SLP data. For many stations, however, data from surrounding stations can be used to fill gaps. We refer to the station subject to gap filling as the "target station." For each target station, we considered all stations within a 400 km radius. Considering 1 month at a time, we calculated the linear correlation between SLP at the target station and each surrounding station. At this point, we only considered surrounding stations that fit at least one of the following criteria: (1) more than 10 years of overlap and a correlation of more than 0.85 with the target station SLP, (2) more than 15 years of overlap and a correlation of more than 0.75 with the target station SLP, or (3) more than 30 years of overlap and a correlation of more than 0.7 with the target station SLP. We ranked qualifying stations by correlation coefficient from high to low. By order of rank, we consecutively used each surrounding station to fill any possible gaps. We filled gaps using the linear relationship between the target and surrounding stations. We repeated this process three more times because each target station, if it received new data, experienced an altered ability to act as a gap-filling surrounding station for other target stations.

After using surrounding stations to fill monthly gaps, we used NCEP2 SLP data to fill monthly gaps from 1979 to 2009. For each target station, we considered each of the nine surrounding NCEP2 grid cells (2.5° spatial resolution) as surrounding stations. As long as there were more than 10 years of overlapping data and correlation was greater than 0.6, we used data from the grid cell with the highest correlation to fill gaps. We used easier criteria for gap filling with the NCEP2 data because the short reanalysis record does not allow for as many years of overlap with the station data, and we were most concerned with capturing directional trends for 1989–2009 to determine whether recent trends in SLP are consistent with trends in precipitation.

After using NCEP2 to fill gaps, we once again used surrounding stations to fill more monthly gaps. Finally, we calculated mean SLP records for JJAS at each station and used surrounding stations to fill gaps in JJAS data. Despite these rather extravagant gap-filling methods and relaxed criteria for using NCEP2 data, we found strong regional SLP signals and strong relationships between SLP and JJAS precipitation in the GHA. These strong relationships testify to the overall reliability of monthly GHCN and NCEP2 SLP data.

See Figs. 14, 15, 16, 17, and 18.

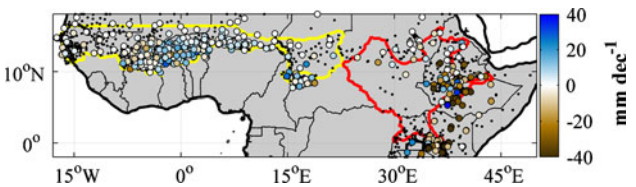

Fig. 14 March–June (MAMJ) precipitation trends. Rate of MAMJ precipitation change between 1970–1989 and 1990–2009 at all gauge locations with at least 10 reported MAMJ precipitation totals during each period. *Black dots* represent gauge locations that do not meet this requirement. The *red polygon* and *yellow polygons* bound the GHA and Sahel regions considered in this study

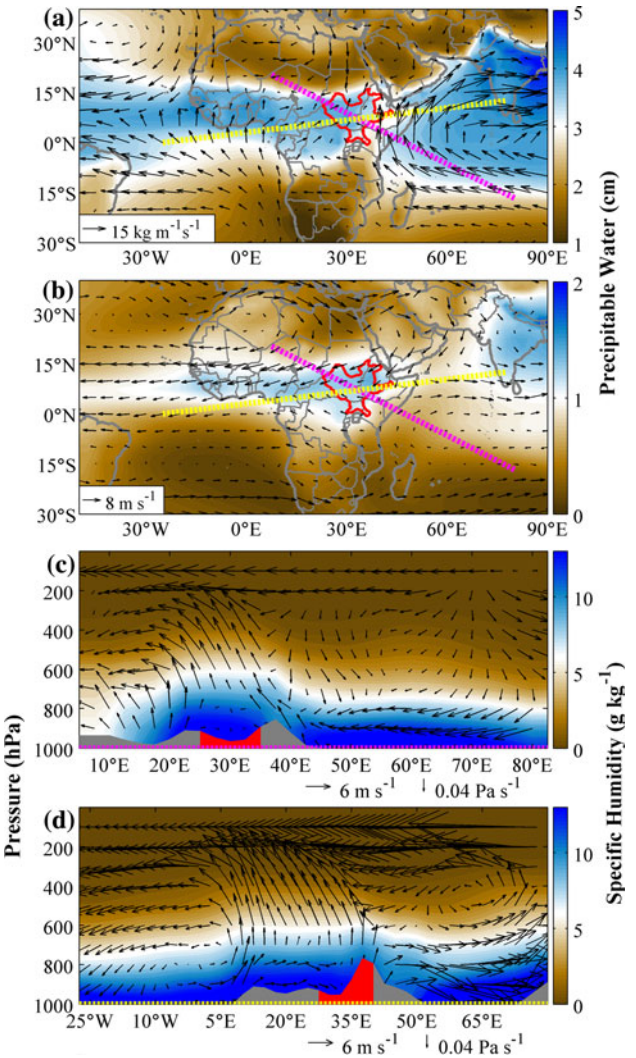

Fig. 15 Mean JJAS atmospheric circulation and moisture transports from 1958 to 2001 according to the ECMWF reanalysis. **a** Lower troposphere below 700 hPa: *arrows* indicate direction and velocity of moisture transports, *background* represents total precipitable water. **b** Mid-troposphere between 700 and 500 hPa: *arrows* indicate direction and velocity of wind, *background* represents total precipitable water. **c** and **d** Vertical profiles of horizontal and vertical wind velocity (*arrows*) and specific humidity (*background*) along the transects defined by the *pink* (**c**) and *yellow* (**d**) *dotted lines* in **a** and **b**. *Grey areas* at the bottom of (**c**) and (**d**) represent land. *Red outlines* in **a** and **b** and *red areas* in **c** and **d** represent the GHA

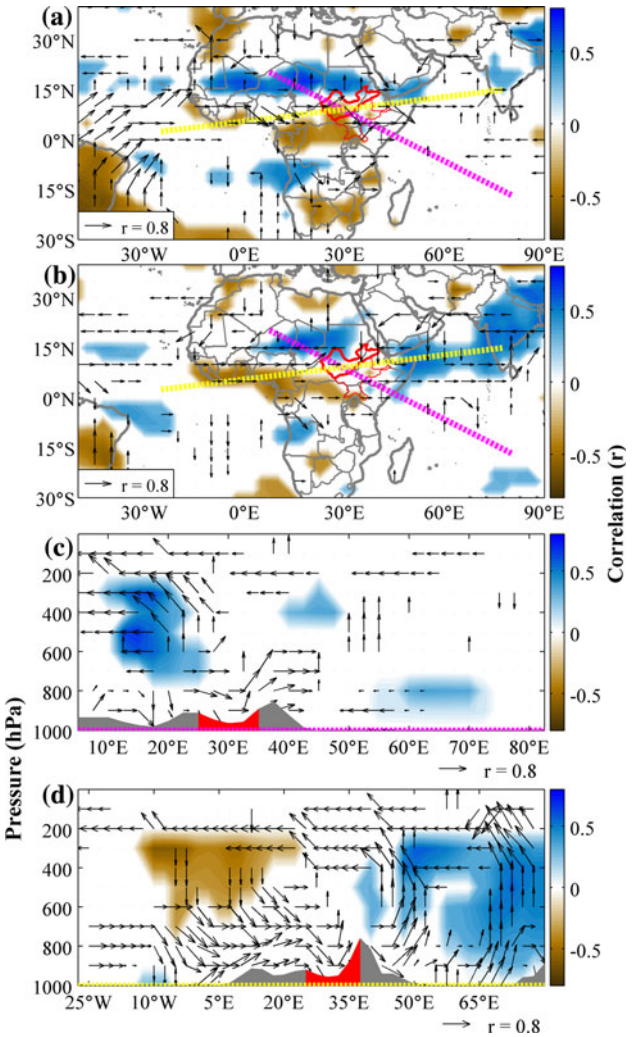

Fig. 16 Correlation between JJAS precipitation in the northern GHA and atmospheric circulation (including moisture transports) from 1958 to 1988 (ECMWF reanalysis). Only correlations exceeding the 90% significance level are shown. **a** Correlation with horizontal moisture transports (*arrows*) and specific humidity (*background*) within the lower troposphere below 700 hPa. **b** Correlation with horizontal wind velocity (*arrows*) and specific humidity (*background*) within the mid-troposphere between 700 and 500 hPa. **c** and **d** Vertical profiles of correlation with horizontal and vertical wind velocity (*arrows*) and specific humidity (*background*) along the transects defined by the *pink* (**c**) and *yellow* (**d**) *dotted lines* in **a** and **b**. *Grey areas* at the bottom of (**c**) and (**d**) represent land. *Bold red outlines* in **a** and **b** and *red areas* in **c** and **d** bound the northern GHA. *Thin red outlines* in **a** and **b** bound the rest of the GHA

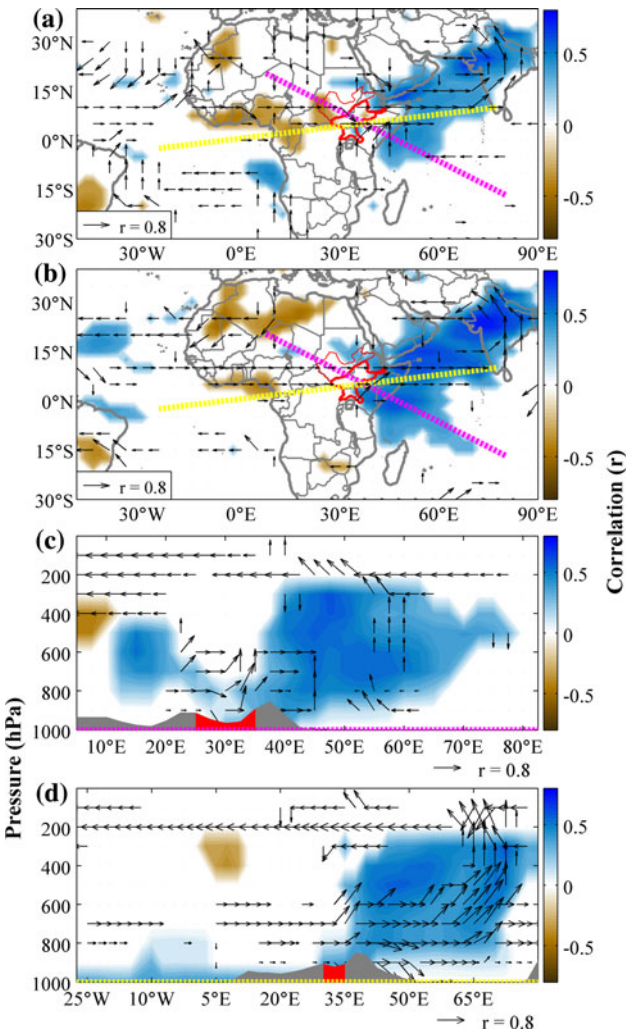

Fig. 17 Correlation between JJAS precipitation in the southern GHA and atmospheric circulation (including moisture transports) from 1958 to 1988 (ECMWF reanalysis). Only correlations exceeding the 90% significance level are shown. **a** Correlation with horizontal moisture transports (*arrows*) and specific humidity (*background*) within the lower troposphere below 700 hPa. **b** Correlation with horizontal wind velocity (*arrows*) and specific humidity (*background*) within the mid-troposphere between 700 and 500 hPa. **c** and **d** Vertical profiles of correlation with horizontal and vertical wind velocity (*arrows*) and specific humidity (*background*) along the transects defined by the *pink* (**c**) and *yellow* (**d**) *dotted lines* in **a** and **b**. *Grey areas* at the bottom of (**c**) and (**d**) represent land. *Bold red outlines* in **a** and **b** and *red areas* in **c** and **d** bound the southern GHA. *Thin red outlines* in **a** and **b** bound the rest of the GHA

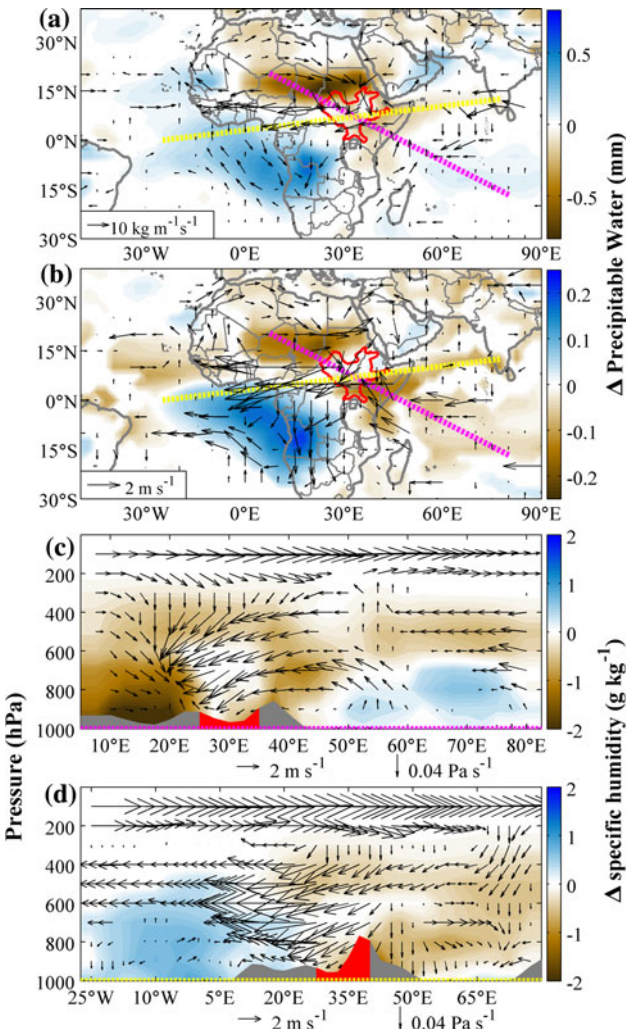

Fig. 18 Change in mean atmospheric circulation and moisture transports between the 1948–1988 period and the 1989–2009 period (NCEP/NCAR reanalysis). Only changes exceeding the 90% significance level according to a 2-tailed student's *t* test are shown. **a** Changes in horizontal moisture transports (*arrows*) and specific humidity (*background*) within the lower troposphere below 700 hPa. **b** Changes in horizontal wind velocity (*arrows*) and specific humidity (*background*) within the mid-troposphere between 700 and 500 hPa. **c** and **d** Vertical profiles of changes in horizontal and vertical wind velocity (*arrows*) and specific humidity (*background*) along the transects defined by the *pink* (**c**) and *yellow* (**d**) *dotted lines* in **a** and **b**. *Grey areas* at the bottom of (**c**) and (**d**) represent land. *Bold red outlines* in **a** and **b** and *red areas* in **c** and **d** represent the GHA

References

Adler RF, Huffman GJ, Chang A, Ferraro R, Xie P, Janowiak J, Rudolf B, Schneider U, Curtis S, Bolvin D, Gruber A, Susskind J, Arkin P (2003) The version 2 Global Precipitation Climatology Project (GPCP) monthly precipitation analysis (1979-present). J Hydrometeorol 4:1147–1167

Allen CD, Macalady AK, Chenchouni H, Bachelet D, McDowell N, Vennetier M, Kitzberger T, Rigling A, Breshears DD, Hogg E, Gonzalez P, Fensham R, Zhang Z, Castro J, Demidova N, Lim J-H, Allard G, Running SW, Semerci A, Cobb N (2010) A global overview of drought and head-induced tree mortality reveals emerging climate change risks for forests. For Ecol Manag 259:660–684

Alory G, Wijffels S, Meyers G (2007) Observed temperature trends in the Indian Ocean over 1960–1999 and associated mechanisms. Geophys Res Lett 34(2):L02606

Anchukaitis KJ, Evans MN (2010) Tropical cloud forest climate variability and the demise of the Monteverde golden toad. Proc Nat Acad Sci 107(11):5036–5040

Bhatt US (1989) Circulation regimes of rainfall anomalies in the African-South Asian monsoon belt. J Clim 2(10):1133–1144

Bonnefille R, Chalié F (2000) Pollen-inferred precipitation time-series from equatorial mountains, Africa, the last 40 kyr BP. Global Planet Change 26(1–3):25–50

Camberlin P (1995) June-September rainfall in North-Eastern Africa and atmospheric signals over the tropics: a zonal perspective. Int J Climatol 15(7):773–783

Camberlin P (1997) Rainfall anomalies in the source region of the Nile and their connection with the Indian summer monsoon. J Clim 10(6):1380–1392

Chen M, Xie P, Janowiak JE, Arkin PA (2002) Global land precipitation: a 50-yr monthly analysis based on gauge observations. J Hydrometeorol 3(3):249–266

Christiansen JH, Hewitson A, Busuioc A, Chen A, Gao X, Held I, Jones R, Kolli RK, Kwon WT, Laprise R, Magaña Rueda V, Mearns L, Menendez CG, Raisanen J, Rinke A, Sarr A, Whetton P (2007) Regional climate projections, ch. 11. In: Solomon S, Qin D, Manning M et al (eds) Climate change 2007: the physical science basis. Contribution of Working Group I to the Fourth Assessment Report of the Intergovernmental Panel on Climate Change. Cambridge University Press, Cambridge, UK, pp 849–940

Cook KH (2008) Climate science: the mysteries of Sahel droughts. Nat Geosci 1(10):647–648

Coplen TB (1995) Discontinuance of SMOW and PDB. Nature 373:285

Dansgaard W (1964) Stable isotopes in precipitation. Tellus 16(4):436–468

De Waal A (1989) Famine mortality: a case study of Darfur, Sudan 1984–5. Popul Stud 42(1):5–24

Dinku T, Connor SJ, Ceccato P, Ropelewski CF (2008) Comparison of global gridded precipitation products over a mountainous region of Africa. Int J Climatol 28(12):1627–1638

Du Y, Xie SP (2008) Role of atmospheric adjustments in the tropical Indian Ocean warming during the 20th century in climate models. Geophys Res Lett 35(8):391–405

Esper J, Frank DC, Battapaglia G, Büntgen U, Holert C, Treydte K, Siegwolf R, Saurer M (2010) Low-frequency noise in δ^{13}C and δ^{18}O tree ring data: a case study of *Pinus unicata* in the Spanish Pyrenees. Glob Biogeochem Cycle 24. doi:10.1029/2010GB003772

Folland CK, Palmer TN, Parker DE (1986) Sahel rainfall and worldwide sea temperatures, 1901–85. Nature 320(6063):602–607

Funk C, Brown ME (2009) Declining global per capita agricultural production and warming oceans threaten food security. Food Sec 1(1):271–289

Funk C, Michaelsen J (2004) A simplified diagnostic model of orographic rainfall for enhancing satellite-based rainfall estimates in data-poor regions. J Appl Meteorol 43:1366–1378

Funk C, Verdin JP (2009) Real-time decision support systems: the famine early warning system network. In: Gebremichael M, Hossain F (eds) Satellite rainfall applications for surface hydrology. Springer, Netherlands, pp 295–320

Funk C, Asfaw A, Steffen P, Senay GB, Rowland J, Verdin JP (2003) Estimating Meher crop production using rainfall in the 'long cycle' region of Ethiopia. FEWS NET Rpecial Report

Funk C, Husak G, Michaelsen J, Love T, Pedreros D (2007) Third generation rainfall climatologies: satellite rainfall and topography provide a basis for smart interpolation. In: Proceedings of the JRC—FAO Workshop, Nairobi, Kenya

Funk C, Dettinger MD, Michaelsen JC, Verdin JP, Brown ME, Barlow M, Hoell A (2008) Warming of the Indian Ocean threatens eastern and southern African food security but could be mitigated by agricultural development. Proc Natl Acad Sci USA 105(31):11081–11086

Funk C, Eilerts G, Verdin J, Rowland J, Marshall M (2011a) A climate trend analysis of Sudan. USGS Fact Sheet, vol 3072. US Geological Survey, Sioux Falls

Funk C, Michaelsen J, Marshall M (2011b) Mapping recent decadal climate variations in Eastern Africa and the Sahel. In: Wardlow B, Anderson M, Verdin J (eds) Remote sensing of drought: innovative monitoring approaches. Taylor and Francis, London

Gat JR, Matsui E (1991) Atmospheric water balance in the Amazon Basin: an isotopic evapotranspiration model. J Geophys Res 96(D7):13179–13188

Gatebe CK, Tyson PD, Annegarn H, Piketh S, Helas G (1999) A seasonal air transport climatology for Kenya. J Geophys Res 104:14237–14244

Gessler A, Brandes E, Buchmann N, Helle G, Rennenberg H, Barnard RL (2009) Tracing carbon and oxygen isotope signals from newly assimilated sugars in the leaves to the tree ring archive. Plant Cell Environ 32(7):780–795

Giannini A, Saravanan R, Chang P (2003) Oceanic forcing of Sahel rainfall on interannual to interdecadal time scales. Science 302(5647):1027–1030

Giannini A, Biasutti M, Verstraete MM (2008) A climate model-based review of drought in the Sahel: desertification, the re-greening and climate change. Global Planet Change 64(3–4):119–128

Gill AE (1980) Some simple solutions for heat-induced tropical circulation. Royal Meteorol Soc Q J 106:447–462

Gill AE (1982) Atmosphere-ocean dynamics, vol 30. International Geophysics Series, Academic Press, San Diego

Grissino-Mayer HD (2001) Evaluating crossdating accuracy: a manual and tutorial for the computer program COFECHA. Tree-Ring Res 57(2):205–221

Hagos SM, Cook KH (2008) Ocean warming and late-twentieth-century Sahel drought and recovery. J Clim 21(15):3797–3814

Hastenrath S (1990) Decadal-scale changes of the circulation in the tropical Atlantic sector associated with Sahel drought. Int J Climatol 10(5):459–472

Hoerling M, Hurrell J, Eischeid J, Phillips A (2006) Detection and attribution of twentieth-century northern and southern African rainfall change. J Clim 19(16):3989–4008

Holmes RL (1983) Computer assisted quality control in tree-ring dating and measurement. Tree-Ring Bull 43:69–78

Hoskins BJ, Rodwell MJ (1995) A model of the Asian summer monsoon. Part I: the global scale. J Atmos Sci 52(9):1329–1340

Journel AG, Huijbregts C (1978) Mining geostatistics. Academic press, London

Jury MR (2010) Ethiopian decadal climate variability. Theor Appl Climatol 101(1):29–40

Kalnay E, Kanamitsu M, Kistler R, Collins W, Deaven D, Gandin L, Iredell M, Saha S, White G, Woollen J (1996) The NCEP/NCAR 40-year reanalysis project. Bull Am Meteorol Soc 77(3):437–471

Kanamitsu M, Krishnamurti T (1978) Northern summer tropical circulations during drought and normal rainfall months. Mon Weather Rev 106:331

Kanamitsu M, Ebisuzaki W, Woollen J, Yang SK, Hnilo JJ, Fiorino M, Potter GL (2002) NCEP-DOE AMIP-II reanalysis (R-2). Bull Am Meteorol Soc 83(11):1631–1643

Kidane A (1989) Demograhic consequences of the 1984–1985 Ethiopian famine. Demography 26(3):515–522

Kucharski F, Bracco A, Yoo JH, Tompkins AM, Feudale L, Ruti P, Dell'Aquila A (2009) A Gill–Matsuno type mechanism explains the tropical Atlantic influence on African and Indian monsoon rainfall. Q J Royal Meteorol Soc 135(640):569–579

Kummerow C, Simpson J, Thiele O, Barnes W, Chang ATC, Stocker E, Adler RF, Hou A, Kakar R, Wentz F (2000) The status of the Tropical Rainfall Measuring Mission (TRMM) after two years in orbit. J Appl Meteorol 39(12):1965–1982

Levin NE, Zipser EJ, Cerling TE (2009) Isotopic composition of waters from Ethiopia and Kenya: insights into moisture sources for eastern Africa. J Geophys Res 114(D23):D23306

Loader NJ, Robertson I, Barker AC, Switsur VR, Waterhouse JS (1997) An improved technique for the batch processing of small wholewood samples to a-cellulose. Chem Geol 136:313–317

Loader NJ, Santillo PM, Woodman-Ralph JP, Rolfe JE, Hall MA, Gagen M, Robertson I, Wilson R, Froyd CA, McCarroll D (2008) Multiple stable isotopes from oak trees in southwestern Scotland and the potential for stable isotope dendroclimatology in maritime climatic regions. Chem Geol 252(1–2):62–71

McCarroll D, Loader NJ (2004) Stable isotopes in tree rings. Quat Sci Rev 23:771–801

Meehl GA, Stocker TF, Collins WD, Friedlingstein AT, Gaye AT, Gregory JM, Kitoh A, Knutti R, Murphy JM, Noda A, Raper SCB, Watterson IG, Weaver AJ, Zhao Z-C (2007) Global climate projections, ch. 10. In: Solomon S, Qin D, Manning M et al. (eds) Climate change 2007: the physical science basis. Contribution of Working Group I to the Fourth Assessment Report of the Intergovernmental Panel on Climate Change. Cambridge University Press, Cambridge, UK, pp 749–845

Mitchell TD, Jones PD (2005) An improved method of constructing a database of monthly climate observations and associated high resolution grids. Int J Climatol 25(6):693–712

Newell RE, Kidson JW (1984) African mean wind changes between Sahelian wet and dry periods. Int J Climatol 4(1):27–33

Nicholson SE (2000) The nature of rainfall variability over Africa on time scales of decades to millenia. Global Planet Change 26(1–3):137–158

Nicholson SE (2005) On the question of the "recovery" of the rains in the West African Sahel. J Arid Environ 63(3):615–641

Nicholson SE (2009a) On the factors modulating the intensity of the tropical rainbelt over West Africa. Int J Climatol 29(5):673–689

Nicholson SE (2009b) A revised picture of the structure of the "monsoon" and land ITCZ over West Africa. Clim Dyn 32(7):1155–1171

Nicholson SE, Grist JP (2003) The seasonal evolution of the atmospheric circulation over West Africa and equatorial Africa. J Clim 16(7):1013–1030

Nicholson SE, Some B, McCollum J, Nelkin E, Klotter D, Berte Y, Diallo BM, Gaye I, Kpabeba G, Ndiaye O (2003) Validation of TRMM and other rainfall estimates with a high-density gauge dataset for West Africa. Part I: validation of GPCC rainfall product and pre-TRMM satellite and blended products. J Appl Meteorol 42(10):1337–1354

Pierce DW, Barnett TP, AchutaRao KM, Gleckler PJ, Gregory JM, Washington WM (2006) Anthropogenic warming of the oceans: observations and model results. J Clim 19(10):1873–1900

Richman MB (1986) Rotation of principal components. J Climatol 6(3):293–335

Riddle EE, Cook KH (2008) Abrupt rainfall transitions over the Greater Horn of Africa: observations and regional model simulations. J Geophys Res 113(D15):D15109

Rinne KT, Boettger T, Loader NJ, Robertson I, Switsur VR, Waterhouse JS (2005) On the purification of α-cellulose from resinous wood for stable isotope (H, C, and O) analysis. Chem Geol 222:75–82

Robertson I, Waterhouse JS, Barker AC, Carter AHC, Switsur VR (2001) Oxygen isotope ratios of oak in east England: implications for reconstructing the isotopic composition of precipitation. Earth Planet Sci Lett 191(1–2):21–31

Roden JS, Ehleringer JR (1999a) Hydrogen and oxygen isotope ratios of tree-ring cellulose for riparian trees grown long-term under hydroponically controlled environments. Oecologia 121(4): 467–477

Roden JS, Ehleringer JR (1999b) Observations of hydrogen and oxygen isotopes in leaf water confirm the Craig-Gordon model under wide-ranging environmental conditions. Plant Physiol 120(4):1165

Roden JS, Lin G, Ehleringer JR (2000) A mechanistic model for interpretation of hydrogen and oxygen isotope ratios in tree-ring cellulose. Geochim Cosmochim Acta 64(1):21–35

Rotstayn LD, Lohmann U (2002) Tropical rainfall trends and the indirect aerosol effect. J Clim 15(15):2103–2116

Rozanski K, Araguas-Araguas L, Gonfiantini R (1996) Isotope patterns of precipitation in the East African region. In: Johnson TC, Odada EO (eds) The limnology, climatology, and paleoclimatology of the East African Lakes. Gordon and Breach Publishers, Newark, pp 79–94

Rudolf B, Schneider U (2005) Calculation of gridded precipitation data for the global land-surface using in-situ gauge observations. In: Proceedings of the 2nd workshop of the International Precipitation Working Group IPWG, Monterey October 2004, EUMETSAT, pp 231–247. ISBN 92-9110-070-6

Salati E, Dall'Olio A, Matsui E, Gat JR (1979) Recycling of water in the Amazon basin: an isotopic study. Water Resour Res 15(5):1250–1258

Segele ZT, Lamb PJ, Leslie LM (2009a) Large-scale atmospheric circulation and global sea surface temperature associations with Horn of Africa June-September rainfall. Int J Climatol 29(8): 1075–1100

Segele ZT, Lamb PJ, Leslie LM (2009b) Seasonal-to-interannual variability of Ethiopian/Horn of Africa monsoon. Part I: associations of wavelet-filtered large-scale atmospheric circulation and global sea surface temperature. J Clim 22(12):3396–3421

Seleshi Y, Zanke U (2004) Recent changes in rainfall and rainy days in Ethiopia. Int J Climatol 24(8):973–983

Smith TM, Arkin PA, Sapiano MRP, Chang C-Y (2010) Merged statistical analyses of historical monthly precipitation anomalies beginning in 1900. J Clim 23(21):5755–5770

Sonntag C, Klitzsch E, Löhnert EP, El-Shazly EM, Münnich KO, Junghans C, Thorweihe U, Weistroffer K, Swailem FM (1979) Palaeoclimatic information from deuterium and oxygen-18 in carbon-14 dated north Saharian groundwaters; groundwater formation in the past. In: Isotope hydrology. International Atmospheric Energy Agency, Vienna, pp 569–581

Stokes MA, Smiley TL (1968) An introduction to tree-ring dating. University of Chicago Press, Chicago

Trenberth KE, Stepaniak DP (2003a) Covariability of components of poleward atmospheric energy transports on seasonal and interannual timescales. J Clim 16(22):3691–3705

Trenberth KE, Stepaniak DP (2003b) Seamless poleward atmospheric energy transports and implications for the Hadley circulation. J Clim 16(22):3706–3722

Uppala SM, KÅllberg PW, Simmons AJ, Andrae U, Bechtold V, Fiorino M, Gibson JK, Haseler J, Hernandez A, Kelly GA, Li X, Onogi K, Saarinen S, Sokka N, Allan RP, Andersson E, Arpe K, Balmaseda MA, Beljaars ACM, Van De Berg L, Bidlot J, Bormann N, Caires S, Chevallier F, Dethof A, Dragosavac M, Fisher M, Fuentes M, Hagemann S, Hólm E, Hoskins BJ, Isaksen L, Janssen PAEM, Jenne R, Mcnally AP, Mahfouf J-F, Morcrette J-J, Rayner NA, Saunders RW, Simon P, Sterl A, Trenberth KE, Untch A, Vasiljevic D, Verterbo P, Wollen J (2005) The ERA-40 re-analysis. Q J Royal Meteorol Soc 131 (612):2961–3012

Verdin J, Funk C, Senay G, Choularton R (2005) Climate science and famine early warning. Philos Trans Royal Soc B Biol Sci 360(1463):2155–2168

Whetton P, Rutherfurd I (1994) Historical ENSO teleconnections in the Eastern Hemisphere. Clim Chang 28(3):221–253

Williams AP, Funk C (2011) A westward extension of the warm pool leads to a westward extension of the Walker circulation, drying eastern Africa. Climate Dynamics. doi:10.1007/s00382-010-0984-y

Willmott CJ, Matsuura K (1995) Smart interpolation of annually averaged air temperature in the United States. J Appl Meteorol 34(12):2577–2586

Wils THG, Robertson I, Eshetu Z, Koprowski M, Sass-Klaassen UGW, Touchan R, Loader NJ (2010) Towards a reconstruction of Blue Nile baseflow from Ethiopian tree rings. The Holocene 20(6):837–848

Wils THG, Robertson I, Eshetu Z, Touchan R, Sass-Klaassen U, Koprowski M (2011) Crossdating *Juniperus procera* from North Gondar, Ethiopia. Trees Struct Funct 25:71–82

Xie P, Arkin PA (1997) Global precipitation: A 17-year monthly analysis based on gauge observations, satellite estimates, and numerical model outputs. Bull Am Meteorol Soc 78(11):2539–2558

Yapp CJ, Epstein S (1982) Climatic significance of the hydrogen isotope ratios in tree cellulose. Nature 297:636–639

Young GHF, Demmler JC, Gunnarson BE, Kirchhefer AJ, Loader NJ, McCarroll D (2011) Age trends in the tree ring growth and isotopic archives: a case study of *Pinus sylvestris* L. from northwestern Norway. Global Biogeochemical Cycles 25. doi:10.1029/2010GB003913

Zimmermann U, Ehhalt DH, Munnich KO (1967) Soil water movement and evapotranspiration: changes in isotopic composition of water. In: Isotopes in hydrology. International Atomic Energy Agency, Vienna, pp 657–585